



8-2014

## Low Temperature Thermally Activated CVD of Silicon on Molybdenum for Oxidation Protection

Brian C. Jolly

University of Tennessee - Knoxville, [bjolly3@vols.utk.edu](mailto:bjolly3@vols.utk.edu)

Follow this and additional works at: [https://trace.tennessee.edu/utk\\_gradthes](https://trace.tennessee.edu/utk_gradthes)



Part of the [Other Materials Science and Engineering Commons](#)

### Recommended Citation

Jolly, Brian C., "Low Temperature Thermally Activated CVD of Silicon on Molybdenum for Oxidation Protection. " Master's Thesis, University of Tennessee, 2014.  
[https://trace.tennessee.edu/utk\\_gradthes/2823](https://trace.tennessee.edu/utk_gradthes/2823)

This Thesis is brought to you for free and open access by the Graduate School at TRACE: Tennessee Research and Creative Exchange. It has been accepted for inclusion in Masters Theses by an authorized administrator of TRACE: Tennessee Research and Creative Exchange. For more information, please contact [trace@utk.edu](mailto:trace@utk.edu).

To the Graduate Council:

I am submitting herewith a thesis written by Brian C. Jolly entitled "Low Temperature Thermally Activated CVD of Silicon on Molybdenum for Oxidation Protection." I have examined the final electronic copy of this thesis for form and content and recommend that it be accepted in partial fulfillment of the requirements for the degree of Master of Science, with a major in Materials Science and Engineering.

George M. Pharr, Major Professor

We have read this thesis and recommend its acceptance:

Thomas R. Watkins, Theodore M. Besmann

Accepted for the Council:

Carolyn R. Hodges

Vice Provost and Dean of the Graduate School

(Original signatures are on file with official student records.)

**Low Temperature Thermally Activated CVD of Silicon on  
Molybdenum for Oxidation Protection**

A Thesis Presented for the

Master of Science

Degree

The University of Tennessee, Knoxville

**Brian C. Jolly**

**August 2014**

Copyright © 2014 by Brian C. Jolly

All rights reserved.

## ACKNOWLEDGEMENTS

I wish to express my sincere thanks and appreciation to all my family and friends. Without their support and encouragement, this work would not have been possible.

I owe thanks to the members of my committee including Dr. George M. Pharr (major professor), Dr. Thomas R. Watkins, and Dr. Theodore M. Besmann for their guidance, teachings, and encouragement.

In addition, I wish to express my gratitude to Dr. James H. Miller for his guidance, and Roberta A. Meisner for her support in performing XRD analysis.

This research was sponsored by the Department Of Energy, National Nuclear Security Administration, under the Global Threat Reduction Initiative's Molybdenum-99 Program, in collaboration with GE-Hitachi.

## ABSTRACT

The United States Global Threat Reduction Initiative (GTRI) is promoting the production of molybdenum-99 without the use of uranium-235. One possible route, called neutron capture technology, is through the activation of molybdenum-98 via irradiation. GE-Hitachi has identified a location within their boiling water reactors for molybdenum-98 irradiation, but the elevated temperatures present, at the location, risk oxidizing the molybdenum. This work explored using a silicon coating to protect the molybdenum from oxidation. With silane gas as the precursor, chemical vapor deposition was employed to produce a silicon coating. Characterization was performed and showed a discrete silicon layer was deposited with little to no inter-diffusion occurring between the coating and the substrate. Oxidation performance was evaluated, and excellent results were observed with the silicon coated specimen having weight gain 3 orders of magnitude less than that of the bare molybdenum.

## TABLE OF CONTENTS

CHAPTER I Introduction and General Information .....	1
CHAPTER II Literature Review .....	4
Chemical Vapor Deposition .....	4
CVD of Silicon .....	4
CVD of Silicon onto Molybdenum.....	7
Oxidation of Molybdenum.....	8
CHAPTER III Experimental procedures .....	9
Materials.....	9
Gases and Substrates .....	9
CVD Equipment.....	11
Furnace .....	11
Gas Delivery .....	15
Process .....	17
Coating Runs.....	18
CHAPTER IV Results and Discussion .....	19
High Deposition Rate Region Determination.....	24
Coating porosity .....	26
Deposition rate .....	29
Deposition efficiency .....	30
EDS Analysis.....	31
XRD Analysis .....	32

Origin of increased deposition rate on outer edge of substrate .....	34
Entry Length Calculations .....	35
Velocity Profile Calculation .....	37
Temperature Profile Calculation .....	40
Deposition Rate Calculation.....	43
Oxidation Performance.....	47
CHAPTER V Conclusions and Recommendations .....	49
LIST OF REFERENCES.....	51
APPENDIX.....	55
Vita.....	60



## LIST OF TABLES

Table 1: Summary of Coating Runs .....	18
Table 2: Distance high deposition rate region persisted from outer edge of specimen. Note: high deposition rate region considered to begin when coating thickness was double that of uniform coating thickness region on the interior of the substrate. ....	26
Table 3: Percent porosity measurements of the silicon coatings located on the outer edge of the substrate nearest coating chamber wall. ....	27
Table 4: Silicon coating thickness measurements and deposition rate calculations.....	30
Table 5: Silicon deposition efficiency (%).....	31

## LIST OF FIGURES

Figure 1: Two different CVD ZrC coatings (~90µm thick) on a graphite composite substrate showing columnar microstructure (top) and an equiaxed microstructure structure (bottom). From [16].	5
Figure 2: Effect of supersaturation and temperature on the structure of vapor deposited materials. After [13]	6
Figure 3: XRD pattern of bare molybdenum substrate. Crystalline silicon and iron was found to be present. Noted on the graph are peaks associated with tungsten and beta radiation.	10
Figure 4: Molybdenum substrate	11
Figure 5: Silicon CVD coating system	12
Figure 6: Close up of furnace and coating chamber	13
Figure 7: Schematic cutaway of coating chamber showing molybdenum substrate and thermocouple position.	14
Figure 8: Gas flow diagram. Note: valves between cross purge and vacuum pump/Ar supply closed during coating run and are only used for evacuation and Ar backfill.	16
Figure 9: Left: Bare substrate; Right: Si coated substrate	20
Figure 10: Typical microstructure on outer edges of substrate closest to furnace wall	20
Figure 11: 400X optical image of Mo-Si-5 taken near center of cross section; CGF .05	21

Figure 12: 400X optical image of Mo-Si-5 taken near edge of cross section; CGF .05.....	21
Figure 13: 400X optical image of Mo-Si-4 taken near center of cross section; CGF .0125.....	22
Figure 14: 400X optical image of Mo-Si-4 taken near edge of cross section; CGF .0125.....	22
Figure 15: 400X SEM image of Mo-Si-7 taken near center of cross section; CGF .0031.....	23
Figure 16: 400X SEM image of Mo-Si-7 taken near edge of cross section; CGF .0031.....	23
Figure 17: 400X SEM image taken at the edge of bottom cross section of Mo-Si-7. Inset shows overall view of the specimen and highlights location of cross section shown. ....	24
Figure 18: High deposition rate region position indicated by red lines. ....	25
Figure 19: Porosity measurement of outer edge coating for Mo-Si-5. Imagine analysis software used to determine porosity based on contrast differences between silicon coating and void space (shown as shaded green area). Porosity determined to be 64 vol% .....	27
Figure 20: Porosity measurement of outer edge coating for Mo-Si-4. Imagine analysis software used to determine porosity based on contrast differences between silicon coating and void space (shown as shaded green area). Porosity determined to be 42 vol% .....	28

Figure 21: Porosity measurement of outer edge coating for Mo-Si-7. Imagine analysis software used to determine porosity based on contrast differences between silicon coating and void space (shown as shaded green area). Porosity determined to be 27 vol% .....28

Figure 22: EDS map of Mo/Si interface; specimen # Mo-Si-7 .....32

Figure 23: Comparison of XRD patterns from the bare molybdenum substrate and the silicon coated substrate (Mo-Si-4). A broadening of the crystalline silicon peak can be seen indicating the deposited silicon material is somewhat amorphous or possibly nano-crystalline. ....33

Figure 24: Calculated radial velocity profile within coating chamber. Green vertical lines represent outer edge of molybdenum substrate and red vertical lines represent the end of high deposition rate area. In between each red and green vertical lines are the lengths reported in Table 2. ....38

Figure 25: Growth rate as a function of temperature showing typical trends in rate limiting reaction regimes. [15] .....39

Figure 26: Mean gas temperature as a function of axial position within the coating chamber. The black vertical line represents the midpoint of the substrate. 42

Figure 27: calculated radial temperature profile across the middle of the substrate. Green vertical lines represent outer edge of molybdenum substrate and red vertical lines represent the end of high deposition rate area. ....44

Figure 28: Adsorption rate as a function of temperature for a 5% blend of silane.  
The red vertical line represents the temperature at which the high deposition rate area began as shown by Figure 27. ....46

Figure 29: EDS map of Mo/Si interface after oxidation testing at 550 °C for 175 hours. [4].....48

Figure 30: 400X SEM image of surface of uncoated moly taken near center of specimen .....56

Figure 31: 1000X SEM image of surface of uncoated moly taken near center of specimen .....56

Figure 32: 1000X SEM image of Mo-Si-7 taken near center of cross section....57

Figure 33: 5000X SEM image of Mo-Si-7 taken near center of cross section....57

Figure 34: 1000X Surface SEM image of Mo-Si-5 taken near center .....58

Figure 35: 5000X Surface SEM image of Mo-Si-5 taken near center .....58

Figure 36: 1000X Surface SEM image of Mo-Si-5 taken near edge .....59

Figure 37: 5000X Surface SEM image of Mo-Si-5 taken near edge .....59

## CHAPTER I

### INTRODUCTION AND GENERAL INFORMATION

Technetium-99m ( $^{99m}\text{Tc}$ ) is a decay product of molybdenum-99 ( $^{99}\text{Mo}$ ) and is the most common medical radioisotope used in ~50,000 diagnostic tests per day. [1] Currently, most  $^{99}\text{Mo}$  is produced by fission of uranium-235 and subsequent processing, which separates the  $^{99}\text{Mo}$  from the other fission products. Due to proliferation concerns, the United States Global Threat Reduction Initiative (GTRI) is promoting the production of  $^{99}\text{Mo}$  without the use of highly enriched uranium. Neutron capture technology is one possible route to accomplish this, which involves the neutron activation of  $^{98}\text{Mo}$  through irradiation within in a nuclear reactor. [2]

GE-Hitachi is keenly interested in neutron capture technology and has identified the traversing in core probe (TIP) tubes in its boiling water reactors (BWRs) as a possible location for  $^{98}\text{Mo}$  irradiation leading to  $^{99}\text{Mo}$  production. However, these facilities have the potential to expose the material to elevated temperatures (>500 °C) which could potentially oxidize the  $^{98}\text{Mo}$  target, causing it to become trapped in the TIP tube and rendering the tube useless.

One approach to circumvent this problem is to coat the molybdenum with an oxygen barrier. Elemental silicon forms a stable oxide layer sufficient to passivate its surface even at elevated temperatures. Silicon coatings can be applied with chemical vapor deposition (CVD) techniques using a variety of precursors, and excellent oxidation protection has been observed even with thin

Si coatings ( $<10\mu\text{m}$ ). [3, 4] However, molybdenum and silicon have the potential to interact and form a molybdenum-silicide compound which is not desirable for post irradiation coating removal. Silicide formation has been detected as low as  $500^\circ\text{C}$ , but does not occur rapidly until  $650^\circ\text{C}$ . [5] Also, molybdenum and silicon have differing coefficients of thermal expansion (CTE) of  $4.8 (10^{-6}/^\circ\text{C})$  and  $2.6 (10^{-6}/^\circ\text{C})$ , respectively. [6] Therefore, a low temperature silicon CVD process is desirable for both minimizing molybdenum-silicide formation and limiting strain induced from CTE mismatch.

Significant work has been done in the field of silicon CVD. However, most of this work has focused on the electronic properties of the silicon coatings with typical deposition temperatures ranging from  $800^\circ\text{C} - 1200^\circ\text{C}$  [7-11] which is required to produce electronic quality coatings using thermally activated CVD techniques. Electronic quality silicon coatings have been produced using plasma enhanced CVD techniques at temperatures below  $500^\circ\text{C}$  [11, 12], but this adds unnecessary complexity and expense as the requirements for silicon coatings for oxidation protection are less demanding, with the primary concern being adherence and continuity.

This research explores utilizing thermally activated chemical vapor deposition to coat the molybdenum substrate with a thin Si layer and determine its effectiveness as an oxidation barrier. The effect of varied gas composition on the Si deposition characteristics at low temperature ( $<600^\circ$ ) is investigated through microstructure analysis. Energy dispersive spectroscopy is used to

evaluate inter-diffusion between the Si coating and molybdenum substrate. Results from thermal/hydrodynamic models estimating temperature and velocity variations within the coating chamber are presented to explain regions of observed high deposition rates. The oxidation performance of the Si coating is evaluated at elevated temperature and compared to that of bare molybdenum.



## CHAPTER II

### LITERATURE REVIEW

#### **Chemical Vapor Deposition**

Chemical Vapor Deposition (CVD) is an important processing technology enabling the formation of many high purity materials such as metals, alloys, intermetallics, carbides, etc. [13] The CVD process involves the formation of solid products through decomposition and then deposition from gaseous reactants. Reactant decomposition is accomplished via an activated environment (i.e., thermal, light, plasma), and deposition occurs with nucleation and growth either on the substrate's surface or in the gas phase, or some combination of both. [10, 14] Processing conditions such as temperature, pressure and gas concentration can be used to control the deposited material's microstructure and properties. Figure 1 shows examples of some of the varied microstructures possible with CVD, and Figure 2 schematically describes the typical effect of temperature and supersaturation of the vapor on microstructure.

#### **CVD of Silicon**

CVD has been used for depositing silicon since 1909, with common use in the electronics industry coming after World War II. [15] Typically, the Si is deposited via thermal CVD or some variation of thermal CVD such as plasma enhanced CVD, hot wire CVD, etc. Precursors usually include chloride-based

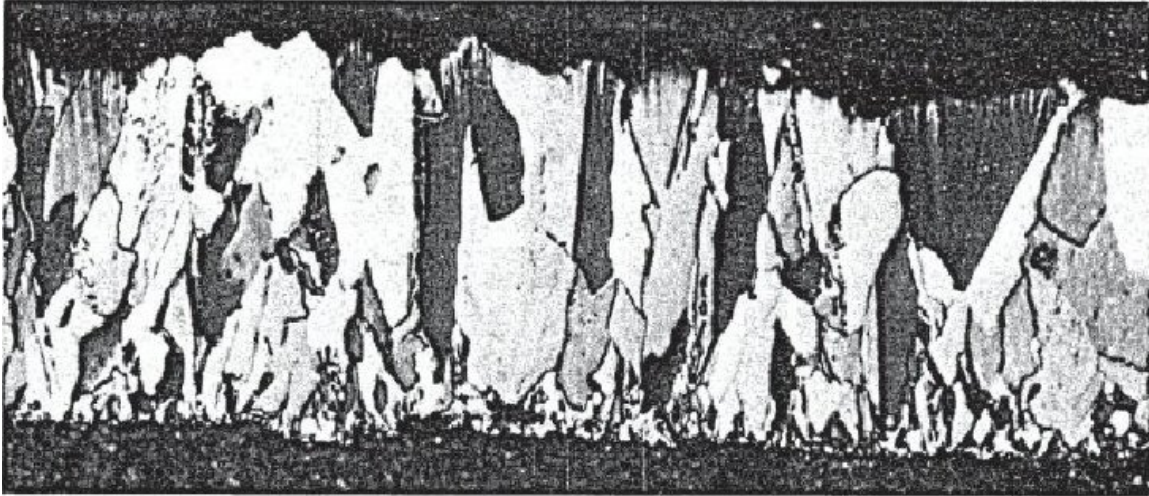


**Figure 1: Two different CVD ZrC coatings (~90 $\mu$ m thick) on a graphite composite substrate showing columnar microstructure (top) and an equiaxed microstructure structure (bottom). From [16]**



**Figure 2: Effect of supersaturation and temperature on the structure of vapor deposited materials. After [13]**

materials (e.g., silicon tetrachloride ( $\text{SiCl}_4$ ), silicon trichlorosilane ( $\text{SiCl}_3\text{H}$ ), etc.) or silane ( $\text{SiH}_4$ , a silicon analogue of methane). [9, 12] Equations 1 - 3 show the general reaction for silicon tetrachloride, silicon trichlorosilane and silane. Note that the  $\text{SiCl}_4$  and  $\text{SiCl}_3\text{H}$  reactions require the addition of hydrogen to combine with the freed chlorine producing  $\text{HCl}$  as a byproduct. The  $\text{SiH}_4$  reaction requires no additional gases and only has hydrogen as a byproduct.

Chloride-based precursors are used to produce high quality, epitaxial Si for semi-conductor devices. [9, 12] However, a high temperature process ( $>1000^\circ\text{C}$ ) is required, which limits the density of devices per chip due to inter-diffusion caused by the elevated temperature. Silane can also be used, which has a lower thermal decomposition temperature and thus a lower deposition temperature, limiting temperature induced interdiffusion. Using a plasma-enhanced CVD process, high quality epitaxial Si coatings can be grown at

600-800 °C with silane. [12] Other microstructures are possible as deposition conditions highly influence crystal structure. By controlling gas composition, temperature, and pressure both polycrystalline and amorphous Si can be produced. [9, 11, 12]



## CVD of Silicon onto Molybdenum

Mo has been used as a temporary, self-releasing, substrate for the growth of polycrystalline silicon for possible use in photovoltaic cells. Rice and Sarma [8] performed silicon deposition experiments on Mo at 1150 °C using SiCl<sub>4</sub> as the precursor and grew 150-250 μm thick Si coatings. Inter-diffusion occurred forming molybdenum silicide, mostly in the form of MoSi<sub>2</sub>. Si, being the primary diffusor, moved into the Mo leaving Kirkendall voids, aiding in the thermal expansion shear separation observed. While the self-releasing nature of this process allows fabrication of polycrystalline sheets, it does not offer a permanent protective Si coating on the Mo.

## Oxidation of Molybdenum

Molybdenum's high melting point and good mechanical properties at elevated temperatures make it and Mo-based alloys attractive high temperature materials. However, poor oxidation resistance limits its applications. Gulbransen et al [17] reported moderate oxidation rates below 450 °C with mass gains of  $\sim 0.015 \text{ mg}\cdot\text{cm}^{-2}\cdot\text{h}^{-1}$  at 425 °C and kinetics following a parabolic rate law. Above 450 °C, however, the oxidation rate increases significantly. [18-20] At 600 °C, thermogravimetric studies have shown weight gains of  $\sim 1.6 \text{ mg}\cdot\text{cm}^{-2}\cdot\text{h}^{-1}$ , a two order of magnitude increase over the mass gain rate at 425 °C. [20]

Mo oxidation results in predominately two oxide forms:  $\text{MoO}_2$  and  $\text{MoO}_3$ . The  $\text{MoO}_2$  forms at the Mo/ $\text{MoO}_3$  interface and does not grow past a small critical thickness of only a few micrometers.  $\text{MoO}_3$  is the primary oxide form growing, as shown by Ag diffusion markers, exclusively by inward diffusion of oxygen through the oxide scale.  $\text{MoO}_3$  is also volatile above  $\sim 550$  °C with evaporation rates becoming significant above  $\sim 650$  °C. [18]

## CHAPTER III

### EXPERIMENTAL PROCEDURES

Silicon coatings were applied to molybdenum substrates using CVD with silane gas as the precursor. Silane derived coatings were used in this work due to the low deposition temperatures possible and the elimination of chlorine attack of the substrate, inherent with the use of chloride containing precursors.

#### Materials

##### *Gases and Substrates*

The precursor gas was a blend of at a 5% SiH<sub>4</sub> / 95% argon. Ultra high purity (UHP) argon (99.999% min. purity) was used as a cover gas during heat up and cool down, and as an additional diluent. Both gases were sourced from Air Liquide. Powder metal derived molybdenum disks were used as substrates for the silicon depositions (See Figure 4). These disks were 25.4mm in diameter and 1.96mm thick with a 1mm hole drilled 2.54mm from the edge to facilitate suspension within the coating chamber. The molybdenum disks were supplied by the sponsor and were used in the as-received condition except for drilling the 1mm hole and cleaning with methanol. X-ray diffraction (XRD) was performed on the molybdenum disks by the Scattering and Thermophysics group at the Oak Ridge National Laboratory and revealed some crystalline silicon and iron (Figure 3). Also seen in Figure 3 are peaks associated with tungsten and beta radiation. The beta peak was not fully filtered out during the data collection, and the

tungsten peak is from tungsten from the electron filament plating out on the copper target.

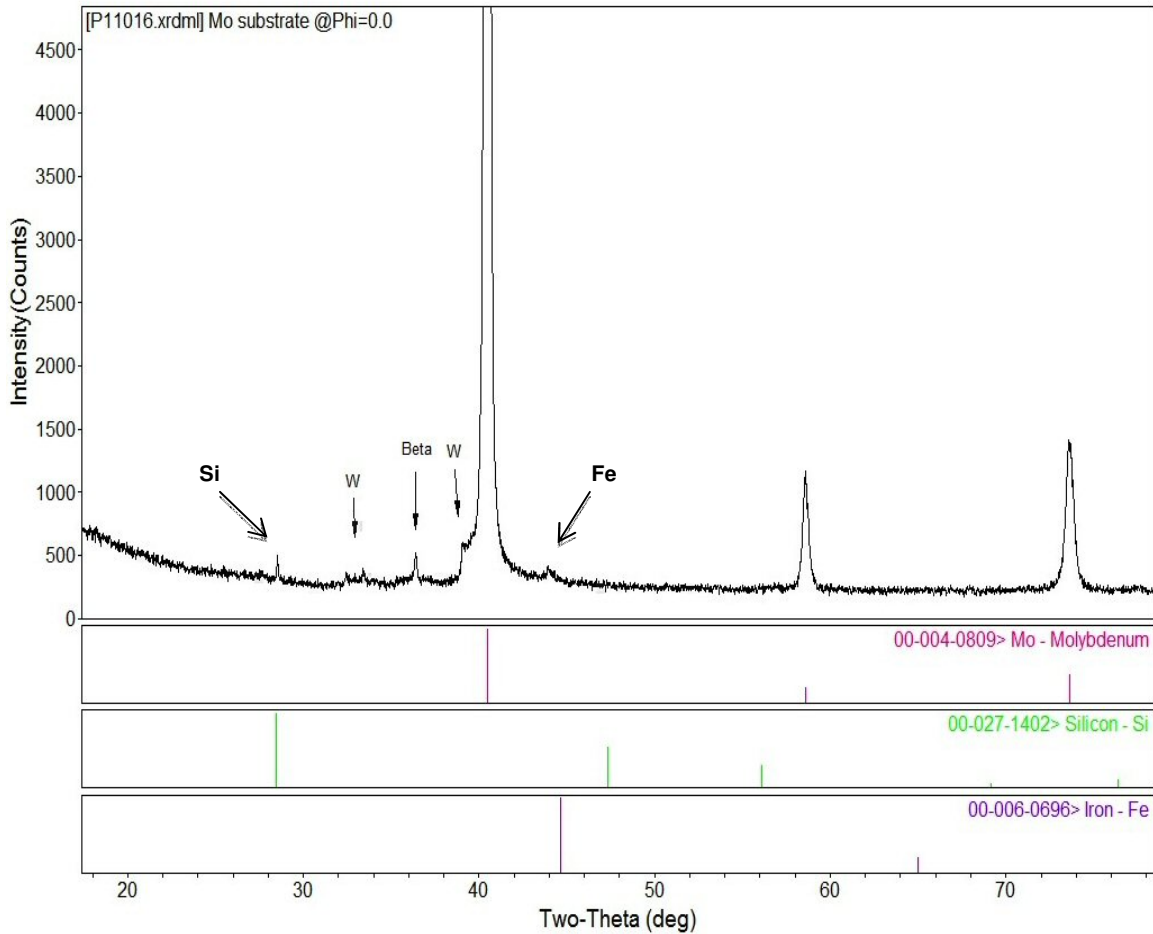


**Figure 3: XRD pattern of bare molybdenum substrate. Crystalline silicon and iron was found to be present. Noted on the graph are peaks associated with tungsten and beta radiation.**

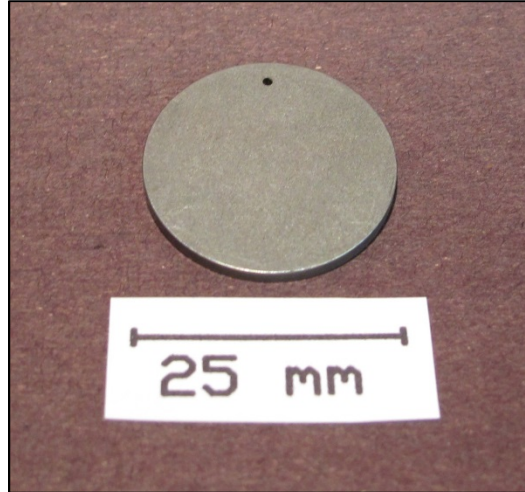


**Figure 4: Molybdenum substrate**

## **CVD Equipment**

### ***Furnace***

Located within a flame resistant hood, a custom designed and built CVD system was used for the silicon coating experiments. The molybdenum substrates were suspended inside a tubular stainless steel coating chamber via a small diameter stainless steel wire. The coating chamber resided in a resistively heated clamshell-type furnace connected to a Honeywell PID process controller\*. Temperature measurements were made utilizing a type K thermocouple located within the coating chamber and positioned near the specimen's midpoint. Figure 5 shows an overall view of the CVD coating system with Figure 6 showing a close up view of the coating chamber identifying the position of the molybdenum substrate. A schematic cutaway of the coating chamber is shown in Figure 7, giving greater detail regarding substrate and thermocouple positioning.

**\*Honeywell UDC model 3300**



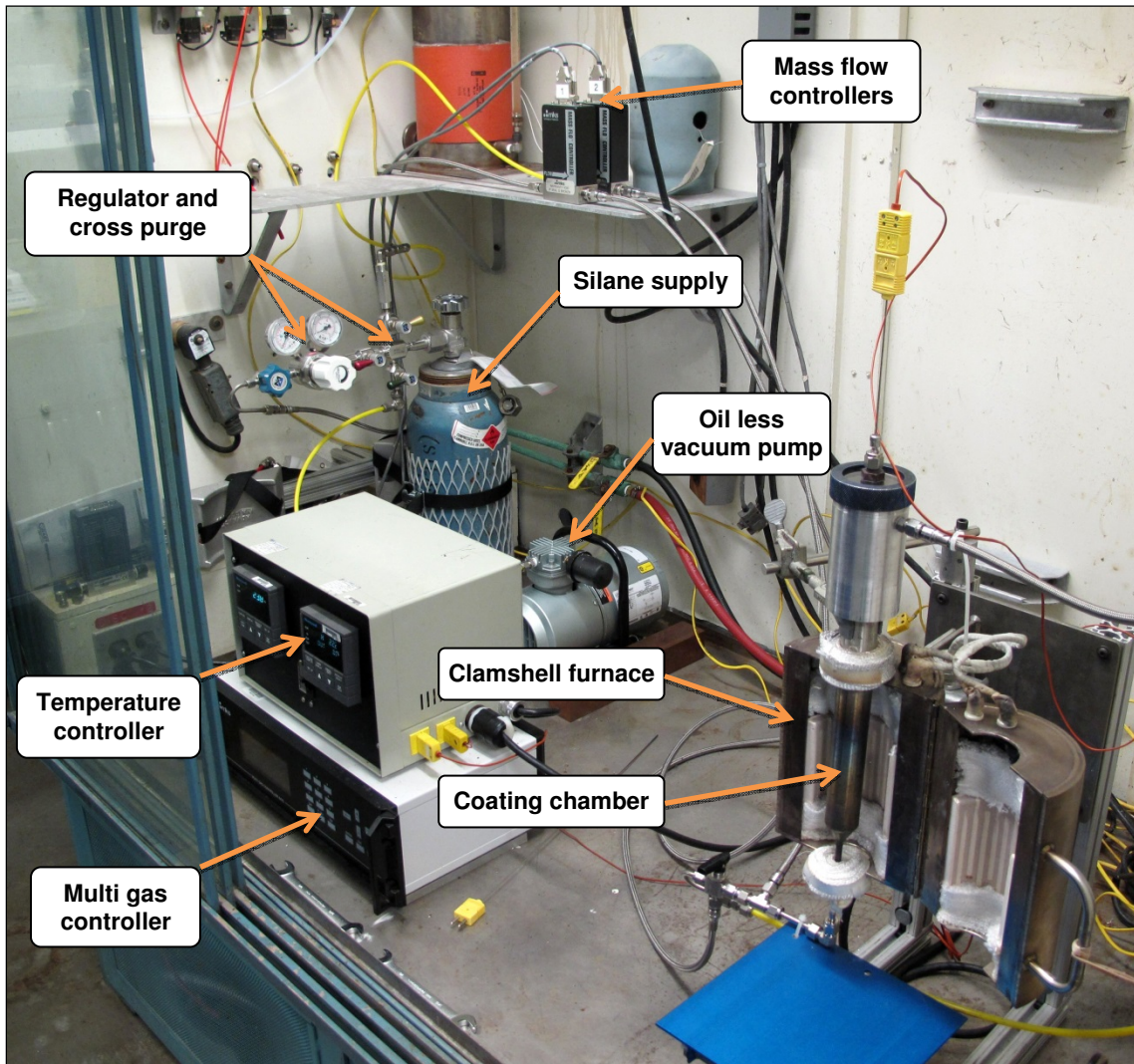


Figure 5: Silicon CVD coating system

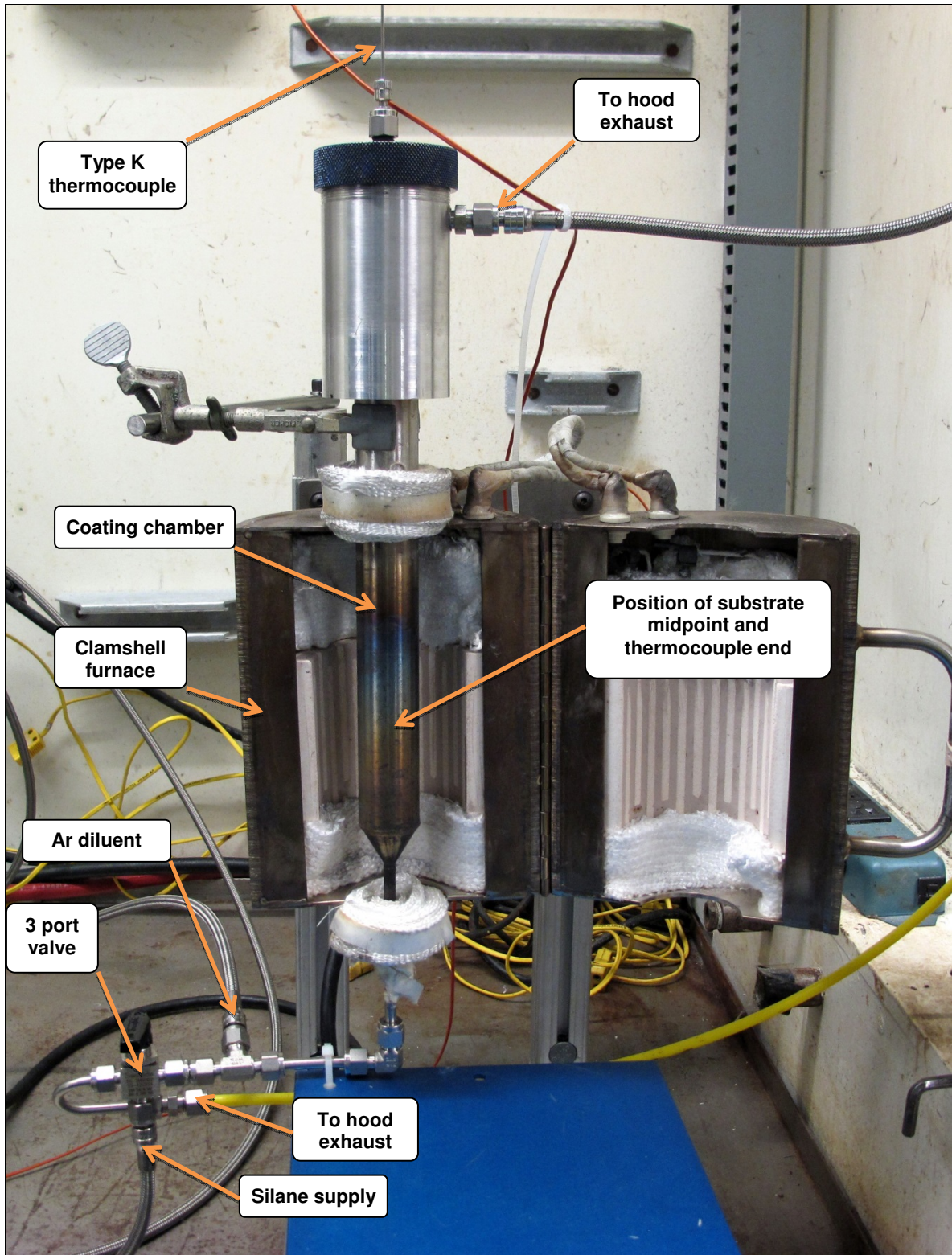


Figure 6: Close up of furnace and coating chamber

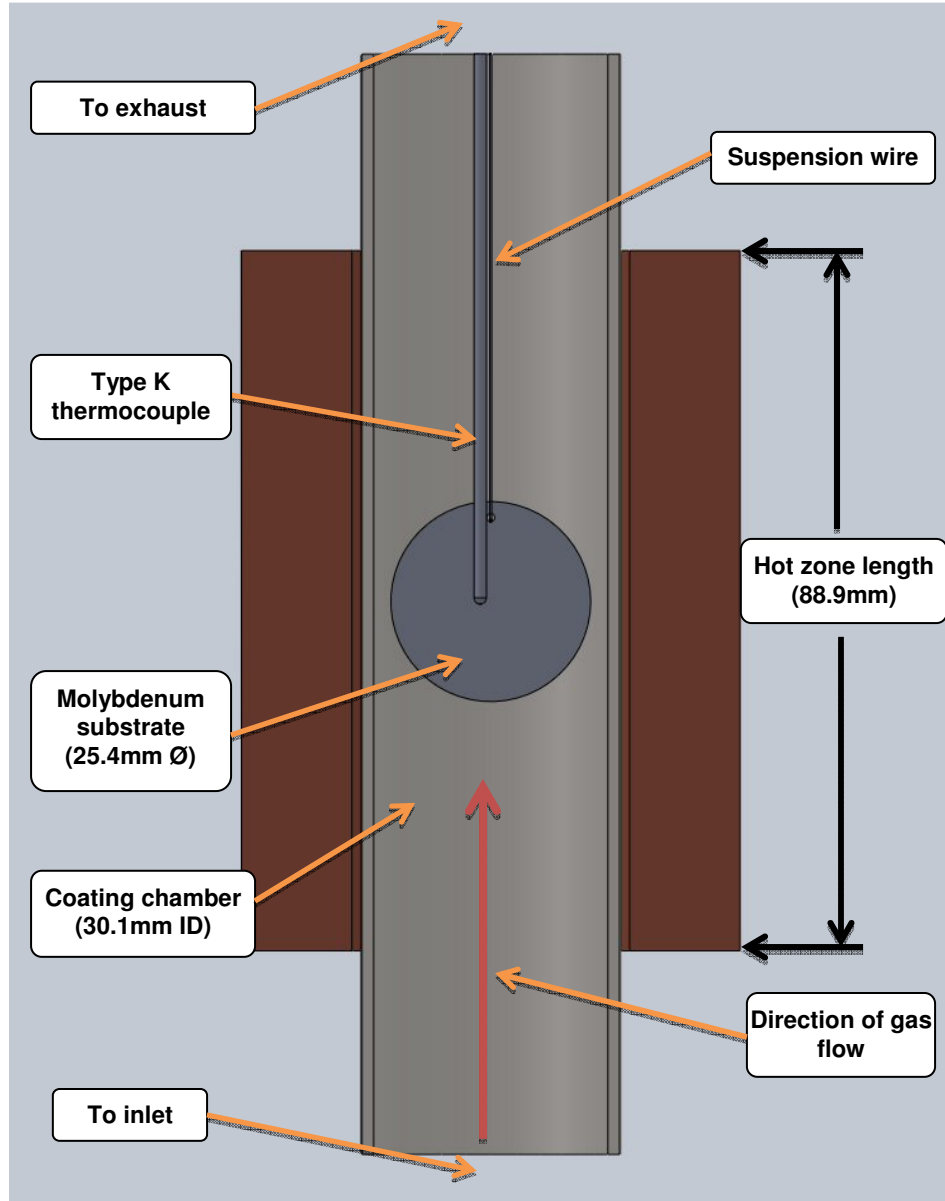


Figure 7: Schematic cutaway of coating chamber showing molybdenum substrate and thermocouple position.

## ***Gas Delivery***

An MKS multi gas controller\*, connected to two MKS mass flow controllers\*\* (MFCs) was used to control gas delivery. One MFC was used to control the supply of 5% silane while the other added pure argon to control the coating gas fraction (CGF). CGF is defined as the ratio of precursor gas flow over total gas flow. The silane was delivered from a gas bottle to the MFC via a cross purge and regulator connected together in series (see Figure 8). The cross purge was attached to an oil-free vacuum pump and UHP argon supply to facilitate evacuation and backfill of all gas delivery components between the silane supply and coating chamber. The evacuation and argon backfill served to eliminate air from the gas delivery components and is required to prevent silane/oxygen interaction leading to silica formation within the system. A three port ball-valve, located just before the coating chamber, was used to direct the silane gas to the hood exhaust until steady state flows were established. Once established, silane flow was switched to the coating chamber. Using this approach, timing of precursor delivery could be more accurately controlled as uncertainty regarding duration required to completely purge the gas delivery system upstream of the coating chamber was eliminated.

**\*MKS model 647C**

**\*\*MKS model 1179A**

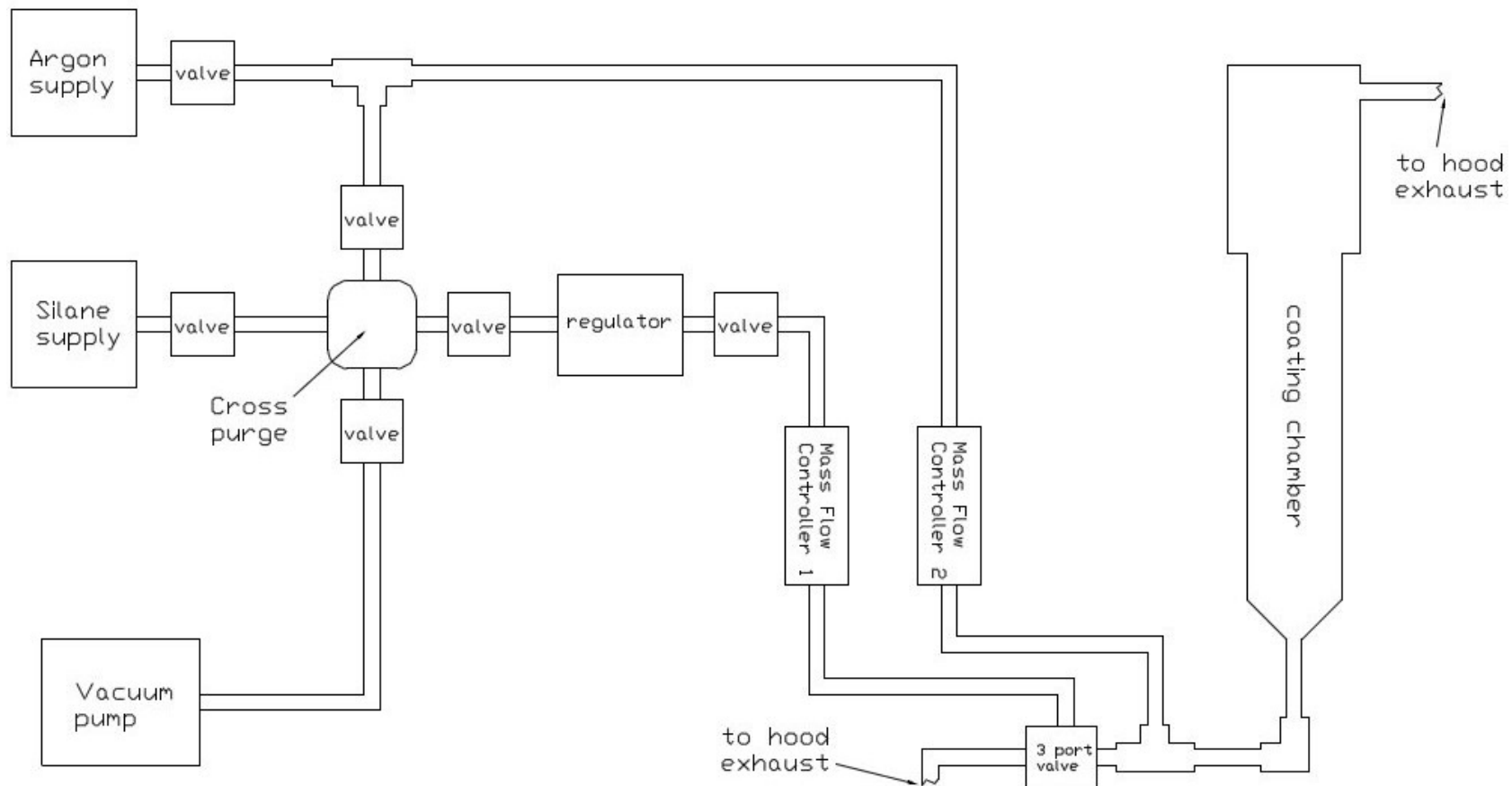


**Figure 8: Gas flow diagram. Note: valves between cross purge and vacuum pump/Ar supply closed during coating run and are only used for evacuation and Ar backfill.**

## Process

The Mo substrate was loaded into the coating chamber, suspended by a stainless steel wire with the attachment points being a small diameter hole drilled through the substrate and an aluminum ring fixed to the upper portion of the thermocouple with a set screw. The position of the substrate within the coating chamber is noted in Figure 6 and Figure 7. The air was purged from the coating chamber by flowing argon through MFC 2 (see Figure 8) for 10 minutes before the system was brought up to the desired coating temperature. Full power was applied to the furnace during heat up which took approximately 1 hour from room temperature. During heat up, air was eliminated from the gas delivery system, between the 3 port valve and silane supply, by a series of 3 repeated evacuation and argon backfill steps. Once at coating temperature, the silane gas flow rate was established while being directed to the exhaust. Once established, silane gas flow was routed to the coating chamber while simultaneously shutting off the argon flow from MFC 2, or adjusting the MFC 2 argon flow if the silane gas was being further diluted. After a predetermined volume of silane had been reacted, the coating run was ended by directing the silane gas flow back to the exhaust and reestablishing the argon purge from MFC 2. Furnace power was shut off, and argon flow was maintained during cool down to room temp. The argon purge was shut off before removal of the coated molybdenum specimen.

## Coating Runs

A summary of the coating experiments is provided in Table 1. All experiments were performed using the previously described procedure with the exception of Mo-Si-1&2. These first two experiments were performed prior to the installation of the 3 port diverter valve, making timing the ending of a run difficult as there was no way to vent silane stored within the volume of the gas delivery system other than flowing it through the coating chamber. Temperature was held constant at 575 °C while CGF was varied for some experiments. Temperature was selected based on previous silicon coating experience. [21]

**Table 1: Summary of Coating Runs**

Experiment #	Time (min)	Total SiH <sub>4</sub> used (cc)	Temp (°C)	Gas flows (sccm)		TGF*** (sccm)	CGF****
				SiH <sub>4</sub> (5%)	Ar		
Mo-Si-1	43	1075	575	500	0	500	0.0500
Mo-Si-2	78	975	575	250	0	250	0.0500
Mo-Si-3*	40	1000	575	500	0	500	0.0500
Mo-Si-4	80	500	575	125	375	500	0.0125
Mo-Si-5	40	1000	575	500	0	500	0.0500
Mo-Si-6**	120	188	575	31.25	468.75	500	0.0031
Mo-Si-7	320	501	575	31.3	469	500.3	0.0031
Mo-Si-8*	40	1000	575	500	0	500	0.0500
Mo-Si-9*	40	1000	575	500	0	500	0.0500

\* submitted for oxidation testing

\*\* MFC stopped up, run aborted

\*\*\* TGF is total gas flow

\*\*\*\* CGF is coating gas fraction

## CHAPTER IV

### RESULTS AND DISCUSSION

Figure 9 shows a typical molybdenum substrate before and after coating with silicon. The silicon coating is fairly uniform on all but the outer left and right edges of the substrate, which were positioned closest to the coating chamber wall. On these outer edges, the coating is considerably thicker showing a high degree of porosity (see Figure 10), indicating a high deposition rate. The average length of these high deposition rate regions was 2.84mm; these measurements are discussed in detail in the following section. Figure 11 - Figure 16 show cross sectional images of the interior and edge areas for coating runs Mo-Si-5, 4, &7, respectively. Note that the figures are ordered to follow the CGF variation between experiments starting with .05 for Mo-Si-5 and decreasing to .0031 for Mo-Si-7. Additionally, higher magnification images of Mo-Si-7 can be seen in the appendix as well as surface images of Mo-Si-5 showing the drastic surface topography differences between the center and edge regions.

Si coatings in the central area appear well bonded to the moly substrate and are high density with thicknesses of 4-9 $\mu$ m. Microstructure of these coatings (Figure 11, Figure 13, and Figure 15) did not vary significantly with CGF, likely because the Si deposition rate at the low coating temperatures is extremely slow. By contrast, the outer edges nearest the coating chamber wall of the cross sections showed significantly thicker coatings with high porosity microstructures that varied with CGF; lower CGF yielded higher densities (Figure 10, Figure 12,



Figure 14 and Figure 16). Experimental temperature mapping of the coating chamber interior was not performed for validation, however thermal modeling was used, and the microstructural differences displayed by these outer left/right edge coatings is thought to be the result of a higher gas temperature region near the coating chamber walls. This will be discussed in further detail later. Cross sectional images of the bottom portion of Mo-Si-7 support this theory showing that the thicker porous coatings aren't just an edge effect (Figure 17).

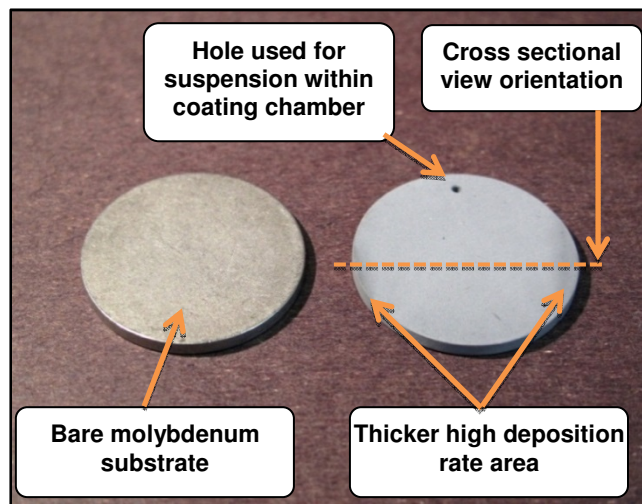


Figure 9: Left: Bare substrate; Right: Si coated substrate

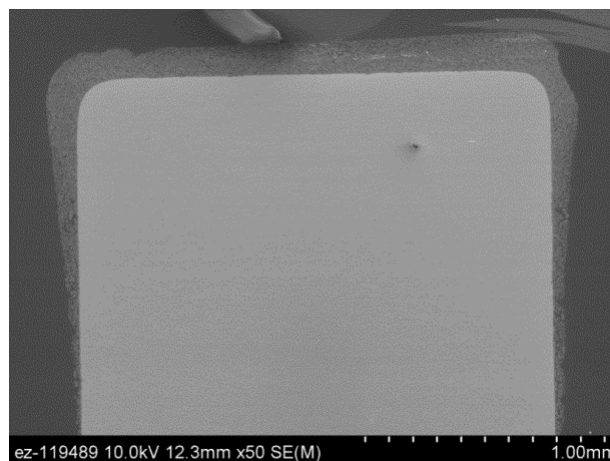


Figure 10: Typical microstructure on outer edges of substrate closest to furnace wall

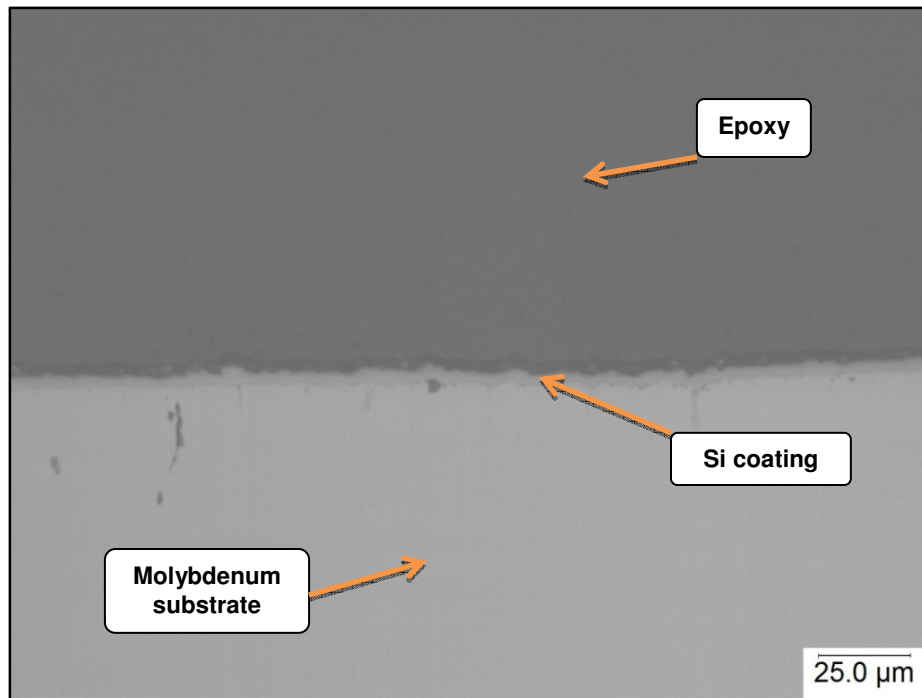


Figure 11: 400X optical image of Mo-Si-5 taken near center of cross section; CGF .05

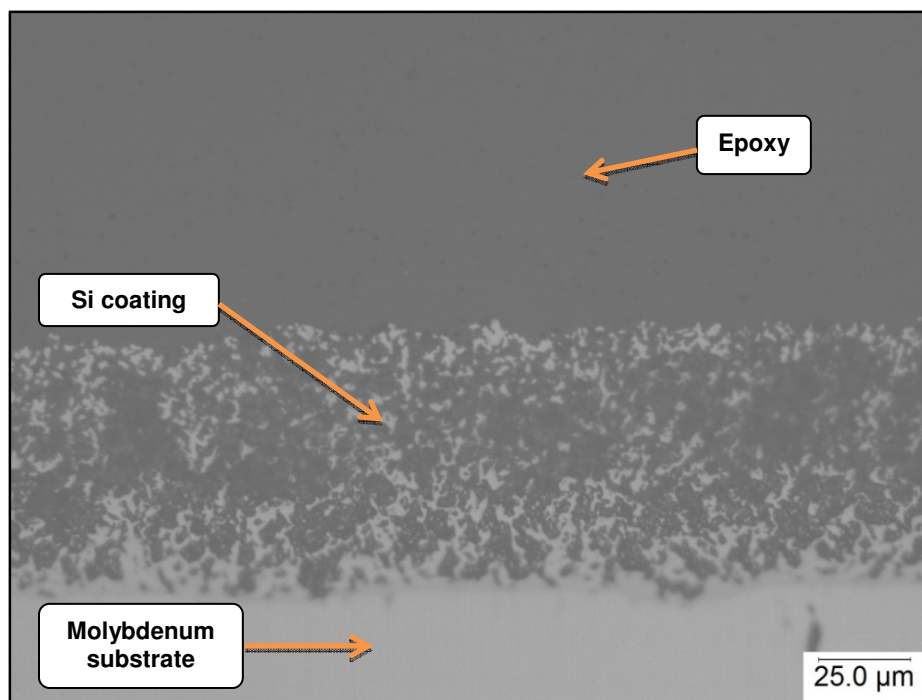


Figure 12: 400X optical image of Mo-Si-5 taken near edge of cross section; CGF .05

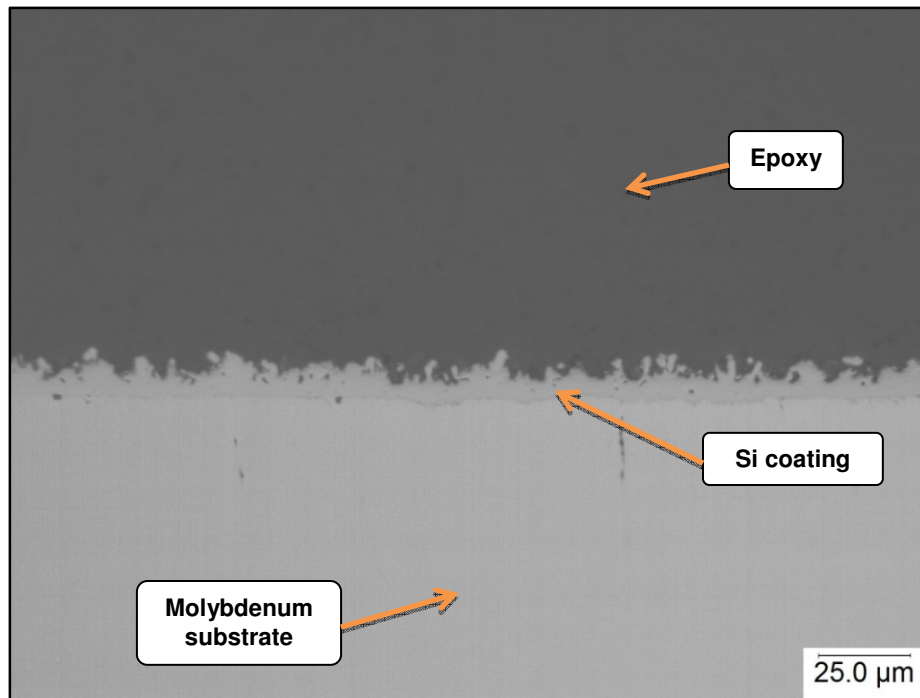


Figure 13: 400X optical image of Mo-Si-4 taken near center of cross section; CGF .0125

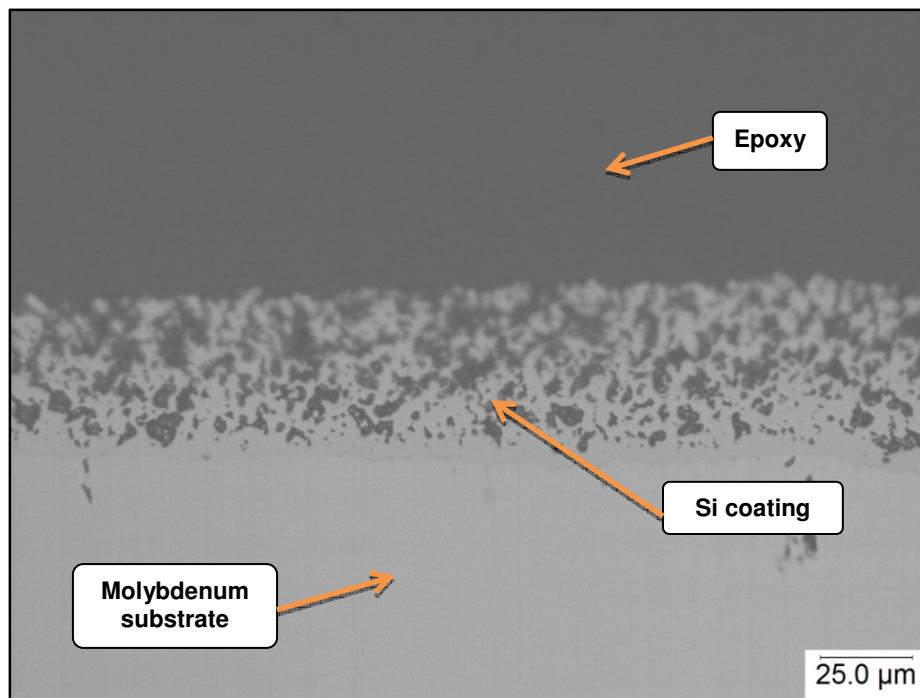


Figure 14: 400X optical image of Mo-Si-4 taken near edge of cross section; CGF .0125

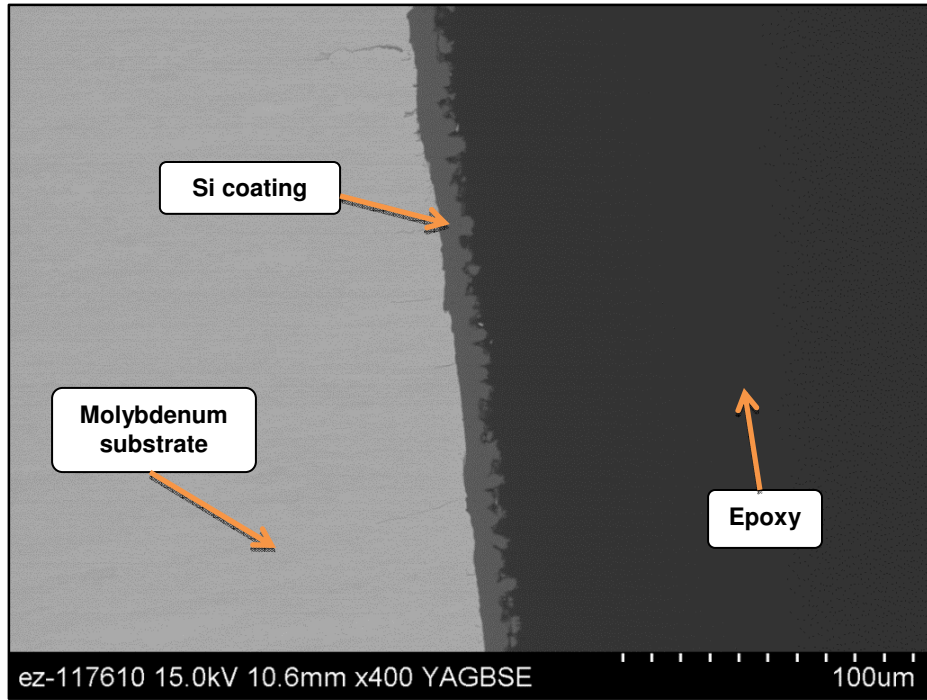


Figure 15: 400X SEM image of Mo-Si-7 taken near center of cross section; CGF .0031

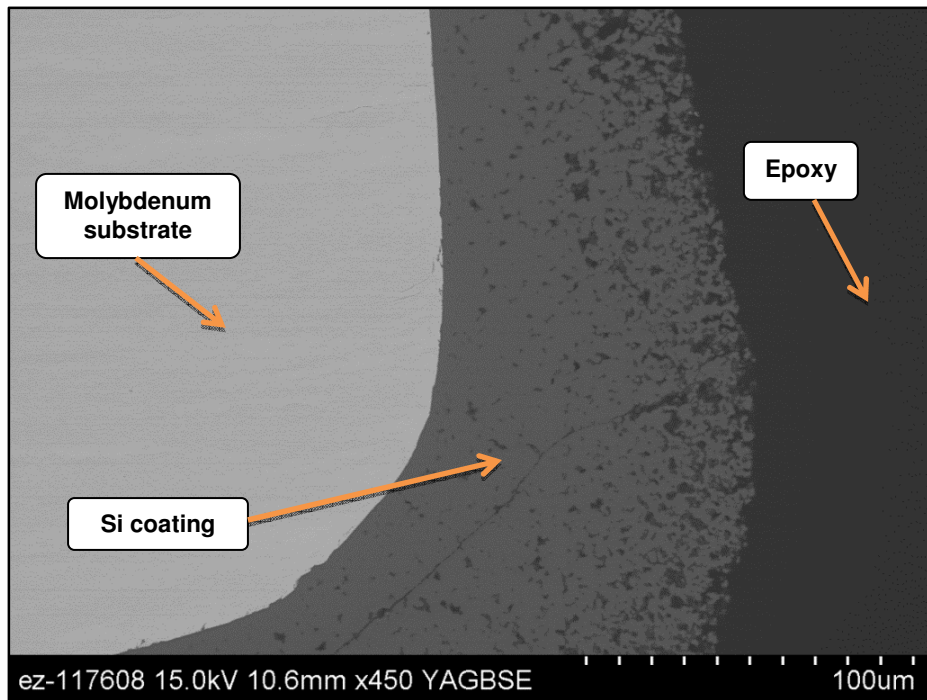
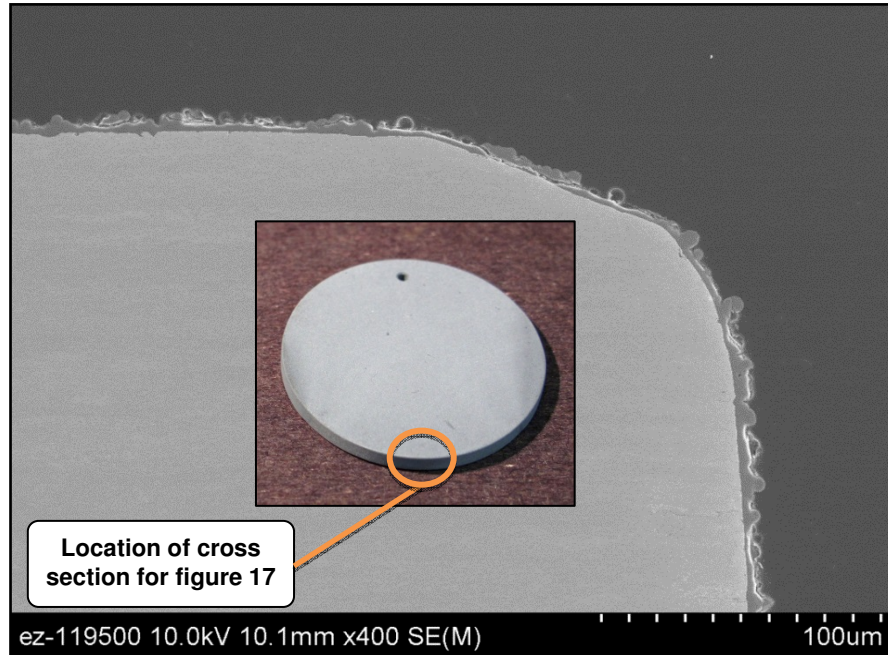


Figure 16: 400X SEM image of Mo-Si-7 taken near edge of cross section; CGF .0031



**Figure 17: 400X SEM image taken at the edge of bottom cross section of Mo-Si-7. Inset shows overall view of the specimen and highlights location of cross section shown.**

## **High Deposition Rate Region Determination**

The lengths of the high deposition rate regions for experiments Mo-Si-4, 5, and 6 are shown in Table 2 with the average being 2.84 mm. The high deposition rate region is considered to begin when the coating thickness was double that of the uniform thickness region in the interior of the substrate. The length is the distance from the beginning of the high deposition rate region to the outer edges of the substrate nearest the coating chamber wall as noted by Figure 18. As these distances were greater than the field of view of the optical microscope used, measurements were made by visually aligning the points to be measured with the left edge of the field of view and measuring the travel of the

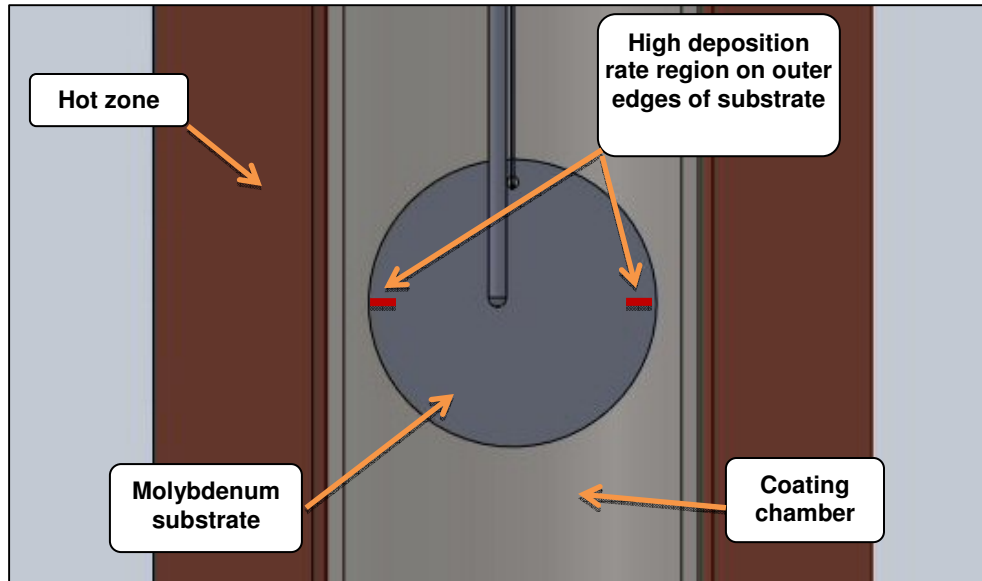


**Figure 18: High deposition rate region position indicated by red lines.**

microscope stage using a dial gauge. Measurements were made from both sides of each substrate to account for any misalignment of the substrate within the coating chamber, and the sides were arbitrary labeled 1 and 2. Lengths of the high deposition rate area for Mo-Si-4 and 7 were fairly uniform between sides 1 and 2, but differed greatly for Mo-Si-5 with side 1 having a distance of 5.46 mm and side 2 being 0 mm. This is likely due to a possible misalignment of the substrate within the coating chamber with the substrate being off center and positioned very near the wall of the coating chamber. If this was the case, this gives a good measurement of how far the high deposition rate region occurs from the coating chamber wall and agrees very well with the measurements from Mo-Si-4 and 7 which were more centered.

**Table 2: Distance high deposition rate region persisted from outer edge of specimen. Note: high deposition rate region considered is to begin when coating thickness was double that of uniform coating thickness region on the interior of the substrate.**

Experiment #	Edge	Distance From Edge (mm)
Mo-Si-4	1	3.18
	2	2.54
Mo-Si-5	1	5.46
	2	0.00
Mo-Si-7	1	2.79
	2	3.05
<b>Average</b>		<b>2.84</b>

## Coating porosity

Porosity of the silicon coating was present predominately on the outer edges of the substrate nearest the coating chamber wall. The percent porosity of the edge coatings shown in Figure 12, Figure 14, & Figure 16, which correspond to Mo-Si-5, 4, and 7, were measured using PAX-it image analysis software. The coating porosity was determined by first masking off the coated area in the micrograph and recording the number of pixels within the mask area. Then, using contrast differences, the image analysis software measures the number of pixels corresponding to void space within the masked off region. The number of pixels corresponding to void space was divided by the total number of pixels within the masked off area and multiplied by one hundred to give percent porosity. Figure 19, Figure 20, & Figure 21 show the area within the micrographs

determined to be void space represented by green shading. The results of the percent porosity measurements are shown in Table 3. Recall that total gas flow and temperature were both held constant for these three experiments and that CGF was the main process variable. It is clear that the CGF impacted the porosity of the edge coatings with lower CGF yielding reduced porosity and higher density coatings.

**Table 3: Percent porosity measurements of the silicon coatings located on the outer edge of the substrate nearest coating chamber wall.**

Experiment #	Time (min)	Total SiH <sub>4</sub> used (cc)	Temp (°C)	CGF	% Porosity (outer edge coating)
Mo-Si-5	40	1000	575	0.0500	64
Mo-Si-4	80	500	575	0.0125	42
Mo-Si-7	320	501	575	0.0031	27

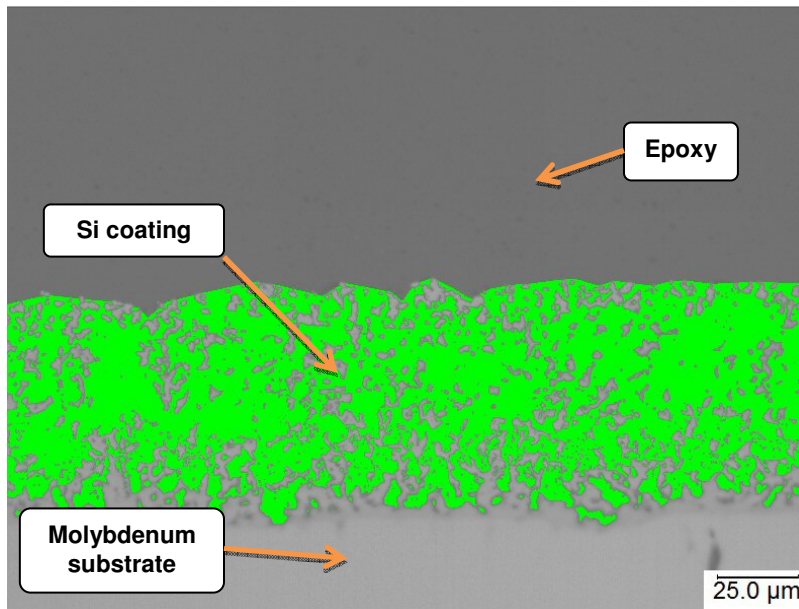


**Figure 19: Porosity measurement of outer edge coating for Mo-Si-5. Imagine analysis software used to determine porosity based on contrast differences between silicon coating and void space (shown as shaded green area). Porosity determined to be 64 vol%**



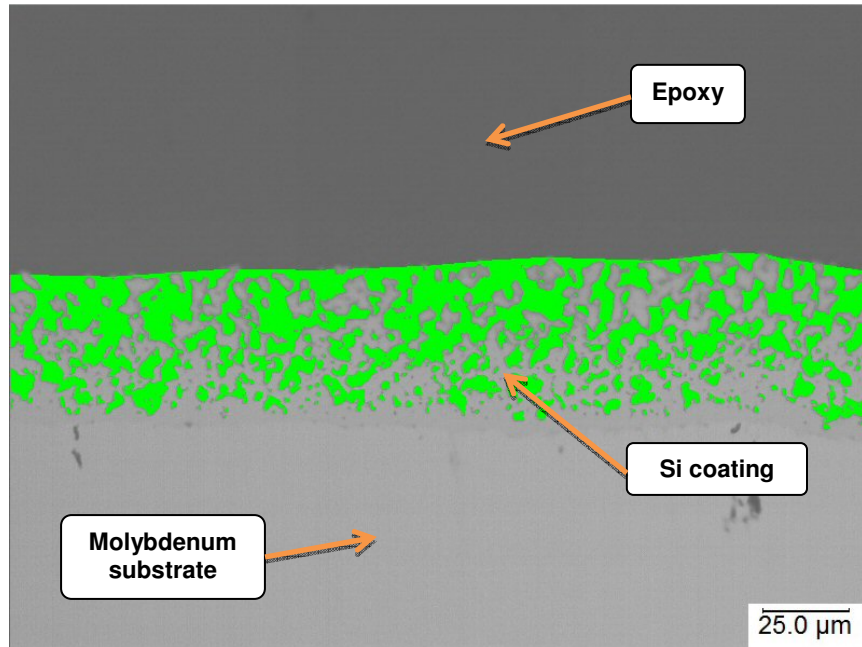


Figure 20: Porosity measurement of outer edge coating for Mo-Si-4. Imagine analysis software used to determine porosity based on contrast differences between silicon coating and void space (shown as shaded green area). Porosity determined to be 42 vol%

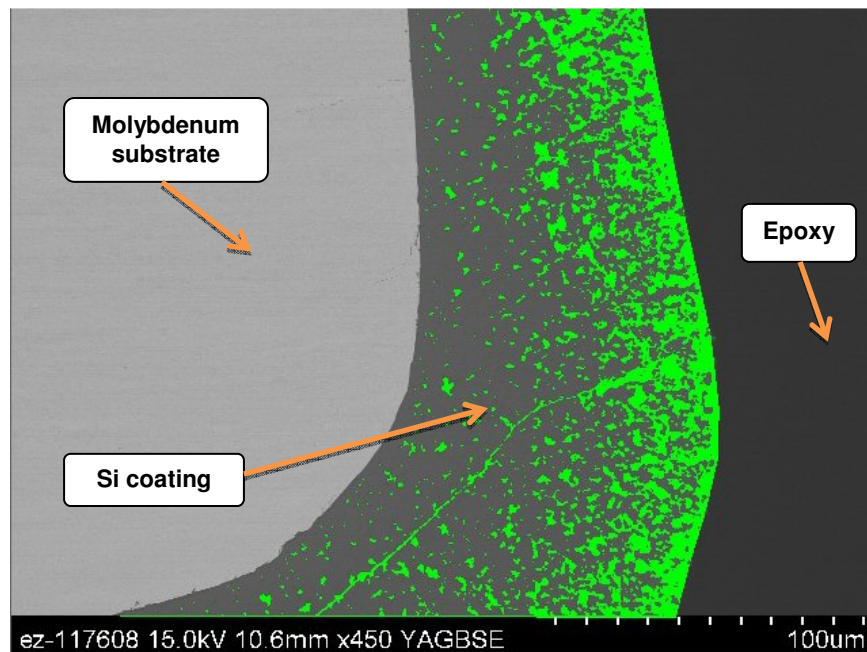


Figure 21: Porosity measurement of outer edge coating for Mo-Si-7. Imagine analysis software used to determine porosity based on contrast differences between silicon coating and void space (shown as shaded green area). Porosity determined to be 27 vol%

## Deposition rate

The deposition rates for coating experiments Mo-Si-4, 5, and 7 were calculated by measuring the silicon coating thicknesses shown in Figure 11 - Figure 16 and dividing by coating duration. Thickness measurements were made using the PAX-it image analysis software. Results of the thickness measurements and deposition rate calculations for the coatings located on the interior, and the outer edges of the substrate are shown in Table 4. Two values for the thickness of the edge coating are given. One is the direct measurement of the edge coating thickness and includes porosity. The second value is the edge coating thickness adjusted to account for porosity and shows the calculated thickness had the coating been 100% dense. The measured porosity values shown in Table 3 were used with equation 4 to calculate the adjusted thickness value for the edge coatings.

$$100\% \text{ Dense thickness} = \text{Porous thickness} \left( 1 - \left( \frac{\% \text{ porosity}}{100} \right) \right) \quad (4)$$

These adjusted thickness values are a better measure of the amount of material deposited and were used to calculate the coating rate on the outer edge of the substrate.

CGF had a strong influence on the interior and edge coating rates with lower CGF producing lower coating rates in both cases. This is not surprising, and is a direct result of the slower delivery of precursor material to the coating

chamber. The coating rates also varied significantly between the interior and outer edge of the substrate with coating rates being on average 5.4 times greater on the edge. Again, this is thought to be the result of higher gas temperatures near the coating chamber walls and will be discussed in detail later.

**Table 4: Silicon coating thickness measurements and deposition rate calculations.**

Experiment #	Time (min)	CGF	Coating Thickness ( $\mu\text{m}$ )		Edge thickness adjusted for porosity ( $\mu\text{m}$ )	Interior coating rate ( $\mu\text{m}/\text{min}$ )	Edge coating rate adjusted for porosity ( $\mu\text{m}/\text{min}$ )
			Interior	Edge			
Mo-Si-5	40	0.0500	4	69	25	0.100	0.625
Mo-Si-4	80	0.0125	7	45	26	0.088	0.325
Mo-Si-7	320	0.0031	9	80	58	0.028	0.181

## Deposition efficiency

Deposition efficiency of the silicon coating experiments was calculated by measuring the coating weight and calculating the weight of silicon introduced to the coating chamber by means of equation 5.  $22400(\text{cc}/\text{mol})$  was used for molar volume of a gas and  $28.09(\text{g}/\text{mol})$  was used for the atomic weight of silicon [22]. Coating weight was determined by measuring the substrate weight before and after coating.

$$\% \text{ efficiency} = \left( \frac{\text{coating weight (g)}}{\left( \frac{\text{silane used (cc)}}{22400 \left( \frac{\text{cc}}{\text{mol}} \right)} \right) \left( 28.09 \left( \frac{\text{g}}{\text{mol}} \right) \right)} \right) \times 100 \quad (5)$$

The results of the deposition efficiency calculations can be seen in Table 5. CGF had an effect on efficiency with lower CGF increasing efficiency from 1.6% to 5.7%. The efficiency for these experiments is relatively low with efficiency reported in the literature as high as ~80% for cold wall reactors and higher deposition temperatures [9]. Several factors contribute to the low deposition efficiency observed in this work; low temperatures used, use of a hot wall reactor leading to co-deposition of silicon on the coating chamber, and a large coating chamber volume/surface area compared to the substrate.

**Table 5: Silicon deposition efficiency (%)**

Experiment #	Time (min)	Total SiH <sub>4</sub> used (cc)	Temp (°C)	CGF	Coating weight (g)	Efficiency (%)
Mo-Si-5	40	1000	575	0.0500	0.0206	1.6
Mo-Si-4	80	500	575	0.0125	0.0223	3.6
Mo-Si-7	320	501	575	0.0031	0.0358	5.7

## EDS Analysis

Energy Dispersive Spectroscopy (EDS) was used to analyze the elemental composition of Mo-Si-7. The EDS map (Figure 22) shows a very distinct interface between the Si coating and the Mo substrate with little to no inter diffusion, indicating that a significant molybdenum silicide layer does not form.

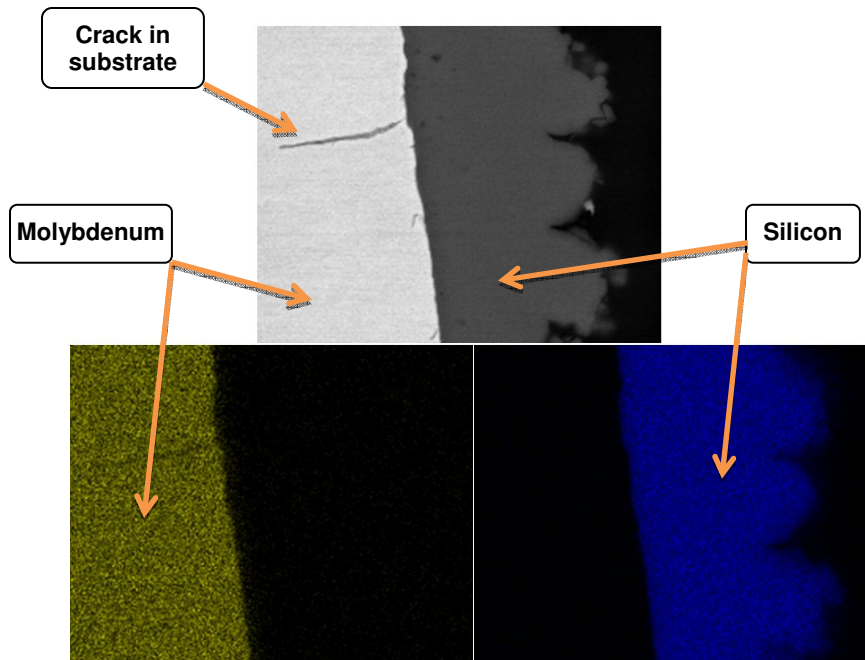
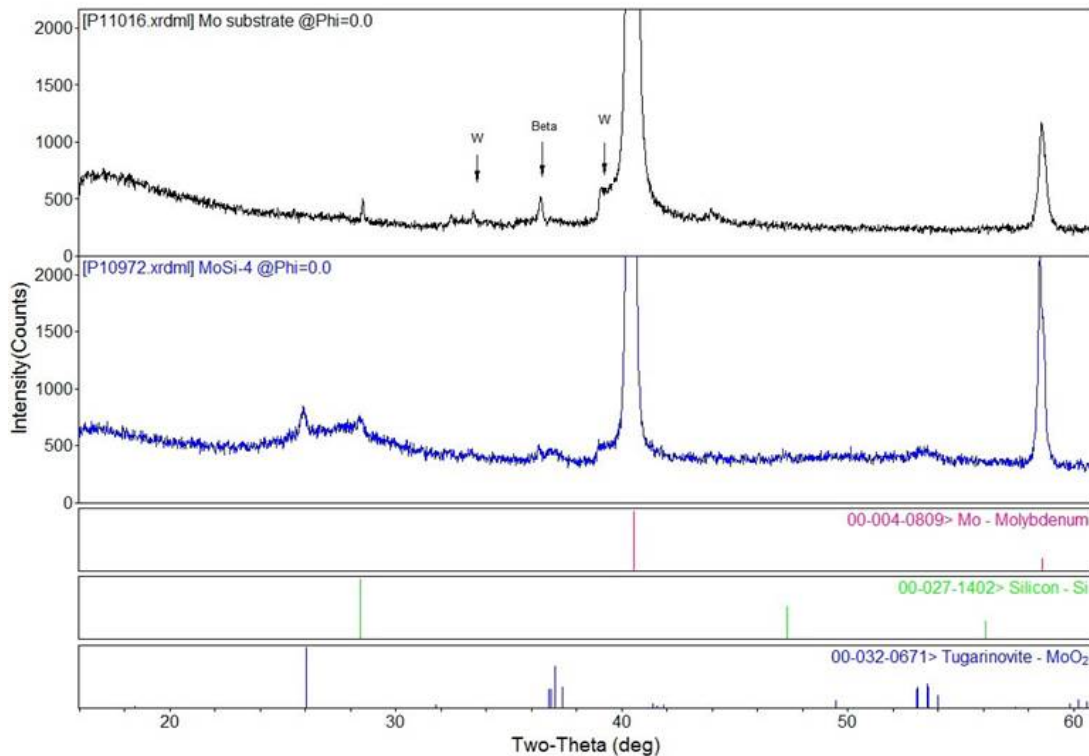


Figure 22: EDS map of Mo/Si interface; specimen # Mo-Si-7

## XRD Analysis

Again, XRD was performed by the Scattering and Thermophysics group on a silicon coated substrate. Mo-Si-4 was chosen as it represented the middle of the range of coating conditions used. Figure 23 shows a side by side comparison of XRD results from the bare molybdenum substrate and Mo-Si-4. As mentioned previously, crystalline silicon and iron are present in the bare molybdenum substrate, and noted in the bare substrate spectra are peaks associated with beta radiation and tungsten from the tungsten filament plated on the copper x-ray target. The XRD data for Mo-Si-4 shows some  $\text{MoO}_2$  present and a broad crystalline silicon peak indicating the silicon deposited is likely either amorphous or nano-crystalline. Further evidence of the structure being either

amorphous or nano-crystalline can be seen in Figure 34 - Figure 37 (located in the appendix) which show the coating surface morphology of Mo-Si-5. On both the interior and edge area of the substrate, the morphology exhibits agglomerations of silicon material rather than the facets of a cubic crystalline structure having long range order. Given the low deposition temperatures used for the silicon depositions in this work, the amorphous/nano-crystalline structure is not surprising. [11, 12] The oxygen source resulting in the MoO<sub>2</sub> formation was likely from either incomplete purging of the coating chamber prior to heat up, or from residual moisture on the surface of the substrate.



**Figure 23: Comparison of XRD patterns from the bare molybdenum substrate and the silicon coated substrate (Mo-Si-4). A broadening of the crystalline silicon peak can be seen indicating the deposited silicon material is somewhat amorphous or possibly nano-crystalline.**

## **Origin of increased deposition rate on outer edge of substrate**

As seen in Figure 10 - Figure 16, the silicon coatings on the edges of the substrates near the furnace wall are highly porous and much thicker compared to the dense coatings on the interior. The porosity accounts for some of the increased thickness, but even taking that into account, it is obvious the silicon deposition rate was much higher on the edges of the substrate near the furnace wall.

Since metallography of a cross section taken from the bottom of a coated substrate revealed dense/uniform silicon coating characteristics similar to that of the middle portion of the substrate (Figure 17), it was assumed a variation in coating conditions at the substrate position within the coating chamber existed in a radial distribution rather than in an axial distribution. (Note: the bottom of the substrate is considered the lowest portion within the coating chamber as illustrated by Figure 7)

Two process variables which can have a large effect on CVD coating characteristics are flow rate of precursor gas and temperature within the coating chamber. Flow rate impacts mass transport processes in the gas phase which carries the precursor to the substrate. [23] Availability of the precursor directly effects coating deposition rate and can have an effect on microstructure. For example, an extremely low flow rate would limit the availability of the precursor (mass transport) leading to low deposition rates and likely dense film or platelet type growth. [13] Temperature also has a large impact on the CVD process by

heavily influencing chemical effects such as thermodynamic and kinetic behavior. [23] Certain phases, for example, are thermodynamically favored over others depending on temperature. Temperature has a significant role in the kinetics of the CVD process giving precursor molecules thermal energy to decompose and the mobility for deposition. Higher temperatures typically yield higher deposition rates.

As the actual flow and temperature distributions of the gas within the coating chamber are difficult to measure experimentally, heat and mass transfer models were used to estimate these profiles.

### ***Entry Length Calculations***

The hydrodynamic and thermal entry lengths are the distances over which the radial hydrodynamic and thermal profiles are developing. Within the entry length, the profiles change as a function of axial position until they become fully developed. The hydrodynamic and thermal entry lengths were calculated for the CVD system using equations 6 and 7 and both the hydrodynamic and thermal profiles were found to be fully developed before the midpoint of the molybdenum specimen. The hydrodynamic and thermal entry lengths were 19.8mm and 13.2mm, respectively, with the midpoint of the molybdenum specimen located 57.15mm into coating chamber and 44.45mm past the start of the heating elements. As silane represented only a small fraction of the gas mixture, a gas composition of 100% argon was used for the thermal and hydrodynamic models



to simplify the calculations. Also, for the thermal entry length calculation, heating was assumed to begin immediately at the start of the heating elements, and axial thermal conduction along the coating chamber was neglected.

For laminar flow (Reynolds number less than 2300), the hydrodynamic entry length ( $x_{fd,h}$ ) is given by [24]

$$x_{fd,h} \approx .05ReD, \quad (6)$$

and, the thermal entry length ( $x_{fd,t}$ ) for laminar flow is given by [24]

$$x_{fd,t} \approx .05RePrD, \quad (7)$$

where  $Re$  is the Reynolds number,  $D$  is the internal diameter of the coating chamber and  $Pr$  is the Prandtl number. For steady state, incompressible flow in a circular tube, the Reynolds and Prandtl numbers are given by [24]

$$Re = \frac{4\dot{m}}{\pi D\mu} \quad (8)$$

$$Pr = \frac{c_p\mu}{k} \quad (9)$$

with  $\dot{m}$ ,  $\mu$ ,  $c_p$ , and  $k$  being mass flow rate, viscosity, specific heat at constant pressure and thermal conductivity, respectively. Viscosity and thermal conductivity values were used for argon at 527 °C. [25] Specific heat at constant

pressure was assumed to be invariant with temperature and data for Ar at 25 °C were used. [26]

### **Velocity Profile Calculation**

With the flow inside the coating chamber determined to be hydrodynamically fully developed, the appropriate solution for calculating the velocity profile was determined. For laminar flow of an incompressible constant property fluid, the radial velocity profile inside a tube is of the form shown by equation 10. [24] Note that the equations used for both the velocity profile shown here and the temperature profile to be discussed later assume a cylindrical geometry and neglect the effect of the substrate within the tube.

$$u(r) = 2u_m \left[ 1 - \left( \frac{r}{r_o} \right)^2 \right] \quad (10)$$

The average velocity ( $u_m$ ) was calculated using the known mass flow rate and evaluated assuming a mean gas temperature of 527 °C.  $r$  and  $r_o$  are the radius at which the flow rate is being evaluated and radius of the tube, respectively.

Figure 24 shows a 2D graph of the radial velocity profile within the coating chamber. The positions within the coating chamber of the outer edge of the molybdenum substrate and the inner bound of the high deposition rate region are shown as vertical lines on the graph with the green line being the edge of the substrate and the red line being the inner bound of the high deposition rate region. The high deposition rate region is considered to begin when the coating

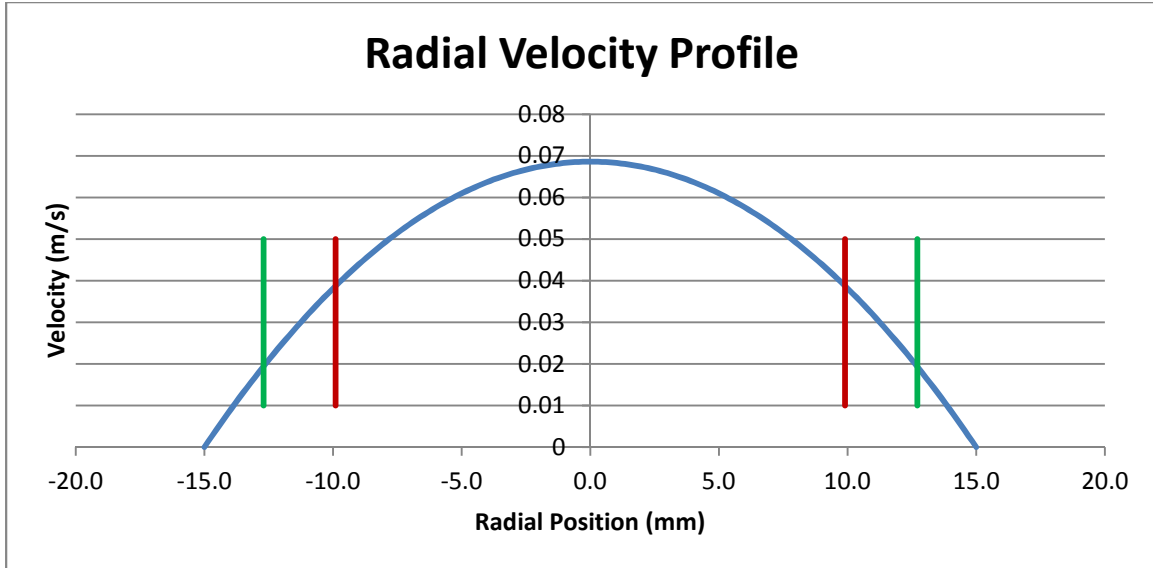


**Figure 24: Calculated radial velocity profile within coating chamber. Green vertical lines represent outer edge of molybdenum substrate and red vertical lines represent the end of high deposition rate area. In between each red and green vertical lines are the lengths reported in Table 2.**

thickness was double that of the uniform thickness region in the interior of the substrate. Details of the length measurement for the high deposition rate region were discussed previously, and the results are shown in Table 2. While there is clearly a large gas velocity variation and therefore a variation in precursor delivery (mass transport), this does not explain the higher deposition rate present on the outer edges of the substrate where the velocity is lowest. This suggests that this process is likely not mass transport limited but kinetics limited, which is consistent with the expectation that surface reaction kinetics, rather than mass transport, is the rate limiting process present at lower temperatures. [15] Figure 25 shows growth rate as a function of deposition temperature (with flow rate fixed) and indicates which rate limiting reaction regime is expected. At low

temperatures, growth rate is controlled by the kinetics of chemical reactions occurring on the substrate surface or in the gas phase, and changes rapidly with temperature. As temperature increases, the kinetics of the chemical reactions become rapid enough to consume the precursor material more quickly than it can be delivered to the substrate surface. At this point, growth rate becomes nearly independent of temperature and is limited by the diffusion (mass transport) of precursor material through the boundary layer to the growth surface. At this point, growth rate becomes nearly independent of temperature and is limited by the diffusion (mass transport) of precursor material through the boundary layer to the growth surface.

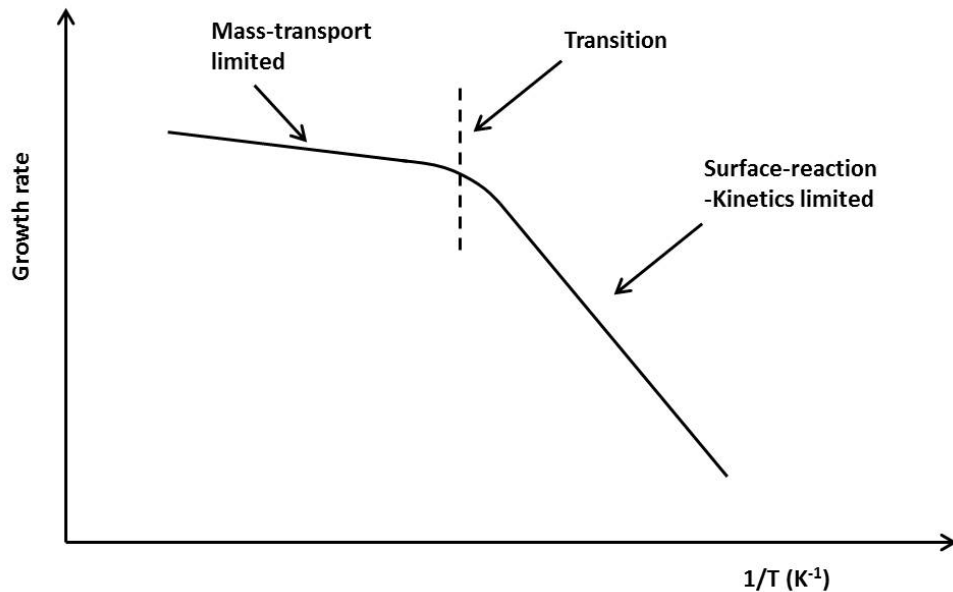


Figure 25: Growth rate as a function of temperature showing typical trends in rate limiting reaction regimes. [15]

## Temperature Profile Calculation

With conditions within the coating chamber shown to be laminar and hydrodynamically/thermally fully developed, assuming negligible axial conduction, the radial gas temperature distribution within a circular tube is given by [24]

$$\frac{1}{r} \frac{\partial}{\partial r} \left( r \frac{\partial T}{\partial r} \right) = \frac{2u_m}{\alpha} \left( \frac{dT_m}{dx} \right) \left[ 1 - \left( \frac{r}{r_o} \right)^2 \right] \frac{T_s - T}{T_s - T_m} \quad (11)$$

Note that equation 11 uses the condition of constant surface temperature of the tube wall. This was thought to be a valid assumption given the extremely slow gas flow rates and the coating chamber being thermally conductive. A solution to the partial differential equation shown in equation 11 can be approximated through the rapidly converging infinite series shown in equation 12. [27, 28]

$$\frac{T_s - T}{T_s - T_m} = \sum_{n=0}^{\infty} C_{2n} \left( \frac{r}{r_o} \right)^{2n} \quad (12)$$

Where  $T_s$  is the surface temperature of the tube,  $T_m$  is the mean gas temperature and  $T$  is the gas temperature at the radial position.  $r$  and  $r_o$  are the radius at which the gas temperature is being evaluated and the radius of the tube, respectively. The coefficients  $C_{2n}$  are given by [27, 28]

$$C_{2n} = \frac{\lambda_0^2}{(2n)^2} (C_{2n-4} - C_{2n-2}), \quad (13)$$

with  $C_0$ ,  $C_2$  and  $\lambda_0$  equal to: [27, 28]

$$C_0 = 1 \quad C_2 = -\frac{\lambda_0^2}{2^2} = -1.828397 \quad \lambda_0 = 2.7043644199$$

For this work, equation 12 was evaluated using  $n=14$  terms. This was found to be more than adequate as, for all practical purposes, equation 13 converged to zero by  $n=10$  thus making equation 12 fully convergent at  $n=10$ .

In order to calculate the radial temperature profile, the mean gas temperature must be determined. Again, assuming a constant surface temperature condition,  $T_m$  as a function of axial position may be calculated using equation 14 [24]

$$\frac{T_s - T_m(x)}{T_s - T_{m,i}} = \exp\left(-\frac{Px}{\dot{m}c_p} \bar{h}\right), \quad (14)$$

where  $P$  is the perimeter of the inside diameter of the coating chamber,  $x$  is the axial position past the beginning of the heating elements at which the mean gas temperature is evaluated and  $\bar{h}$  is the average convection heat transfer coefficient. For use in equation 14, the variation of the convection heat transfer coefficient through the thermally developing region was neglected and  $\bar{h}$  was calculated using the dimensionless Nusselt number ( $Nu$ ) corresponding to the fully developed region using equation 15. [24]

$$T_s = \text{constant} \quad Nu \equiv \frac{hD}{k} = 3.66 \quad (15)$$

where,  $h$  is the convection heat transfer coefficient,  $D$  is the inside diameter of the coating chamber and  $k$  is the thermal conductivity. As before, thermal conductivity data were used for Ar at 527°C. [25]

Using equations 14 and 15, the mean gas temperature at the midpoint of the molybdenum substrate ( $x = 44.45\text{mm}$ ) was calculated to be 528°C. Figure 26 shows the mean gas temperature within the coating chamber as a function of axial position. The black vertical line represents the midpoint of the substrate.

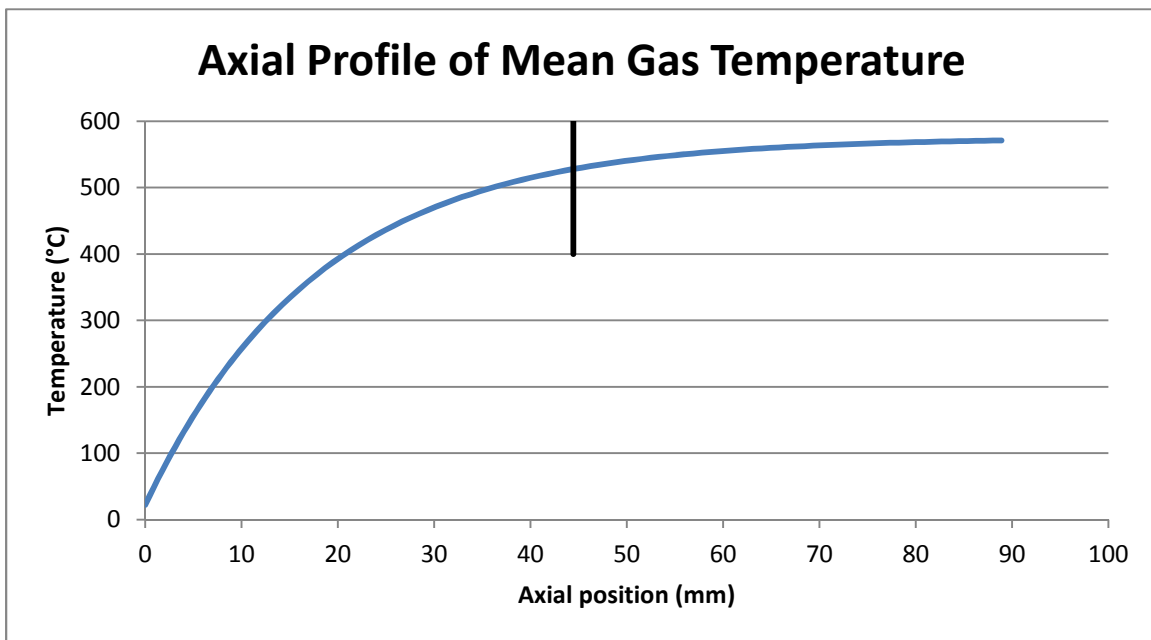


**Figure 26: Mean gas temperature as a function of axial position within the coating chamber. The black vertical line represents the midpoint of the substrate.**

The surface temperature of the inside diameter of the coating chamber was measured experimentally with a type K thermocouple and found to be 575°C. This, in conjunction with the calculated value for the mean gas

temperature was used with equation 12 to calculate the radial temperature profile within the coating chamber at the substrate midpoint (Figure 27). The green vertical lines represent the position of the outer edges of the substrate within the coating chamber (assuming the substrate is perfectly centered) and the red vertical lines represent the average distance from the substrate's edge that the high deposition rate region was observed (Table 2). Again, the high deposition rate region is considered to begin when the coating thickness was double that of the uniform thickness region in the interior of the substrate. As can be seen from the graph, a large gas temperature variation is present throughout the coating chamber with the minimum at the center and maximum at the chamber walls. And, for this study, at temperatures above 555 °C the high deposition rate region begins. Temperature directly affects the kinetics of a CVD reaction with higher temperatures resulting in increased deposition rates, which is consistent with the results from the Si deposition experiments.

### ***Deposition Rate Calculation***

Assuming the Si deposition under consideration is a first order reaction which is rate limited by adsorption of  $\text{SiH}_4$  to the surface of the substrate [29, 30], the deposition rate can be modeled using the kinetic theory of gases and activation energy information. [22, 31] Note that deposition rate and adsorption rate are not the same thing. However, if adsorption rate is the rate limiting step



in the deposition process, deposition rate will be directly proportional to adsorption rate.

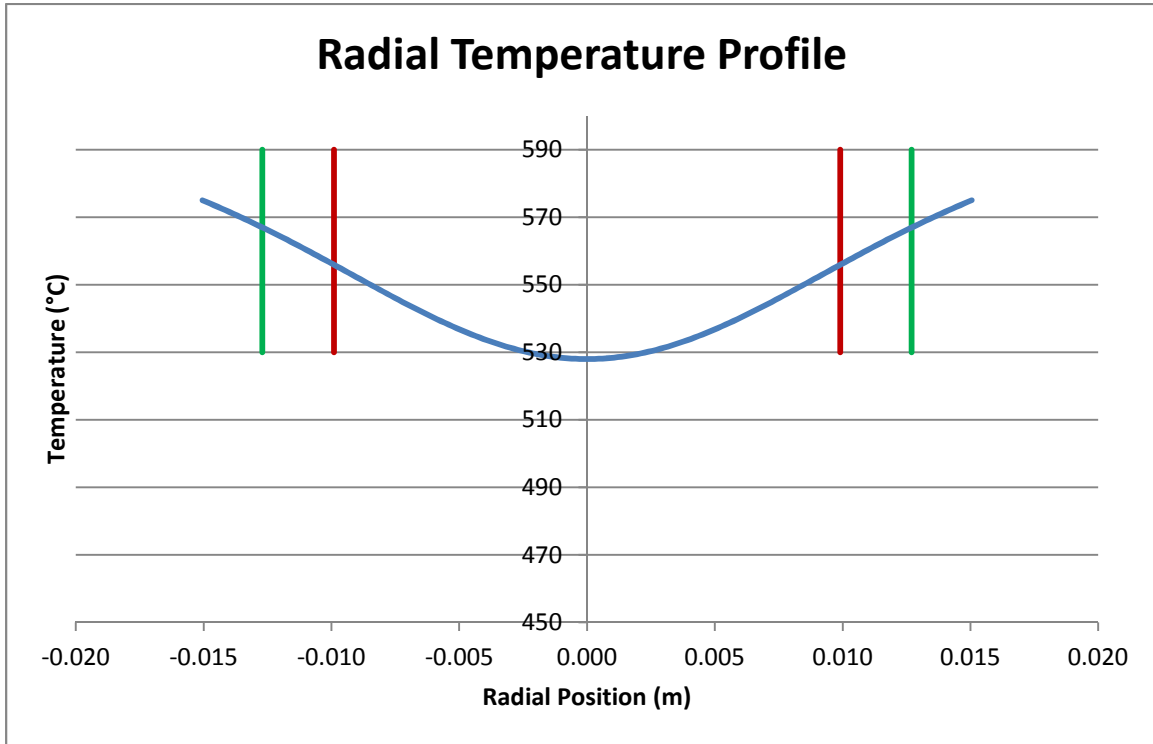


Figure 27: calculated radial temperature profile across the middle of the substrate. Green vertical lines represent outer edge of molybdenum substrate and red vertical lines represent the end of high deposition rate area.

The deposition of molecular species onto a surface is assumed to be the result of collisions between thermally activated molecules and the surface (reaction (16)). If the molecules are thermally activated above the critical activation energy ( $E_A$ ) required for deposition, they will be adsorbed and deposit when they strike the substrate. Otherwise they will return into the gas phase after the collision.



From kinetic theory, the number of collisions of B molecule with a surface, per surface area, per time is given by [22, 31]

$$Z_{Wall} = \left( \frac{kT}{2\pi m_B} \right)^{\frac{1}{2}} \frac{n_B}{V} \quad (17)$$

where  $k$  is Boltzmann's constant,  $T$  is absolute temperature,  $m_B$  is the mass of molecule,  $n_B/V$  is the number of  $B$  molecules per volume. Again, assuming that the adsorption is thermally activated with an activation energy of  $E_A$ , the number of  $B$  molecules adsorbed onto the surface ( $n_{Ad}$ ), per surface area, per time is given by [22, 31]

$$n_{Ad} = Z_{Wall} \exp\left(-\frac{E_A}{RT}\right) \quad (18)$$

with  $R$  being the molar gas constant. Using a value of 125.5 kJ/mol, from the literature [29], for the activation energy of  $\text{SiH}_4$  adsorption, and a value of  $n_B$  corresponding to a 5% blend of  $\text{SiH}_4$ , equation 18 predicts the adsorption rate as a function of temperature shown in Figure 28. The vertical red line indicates the temperature at which the high deposition rate area began. As can be seen, this is in good agreement with the temperature at which the model predicts a large increase in adsorption rate. Also, evaluating the adsorption rate difference at the temperatures predicted for the outer edge of the substrate and the interior portion of the substrate shows a predicted increase of 6.6 times. This is in reasonably good agreement with the experimentally measured deposition rate change which

averaged at an increase of 5.4 times between the outer edge and interior portion of the substrate.

It is worth noting that equation 18 neglects the effects of desorption of  $\text{SiH}_4$  from the substrate surface, giving the impression that the adsorption rate as shown by Figure 28 increases indefinitely. In reality, at high temperatures desorption becomes significant and balances adsorption, thereby limiting deposition rate [15]. However, at the relatively low temperatures under consideration, neglecting desorption is considered valid.

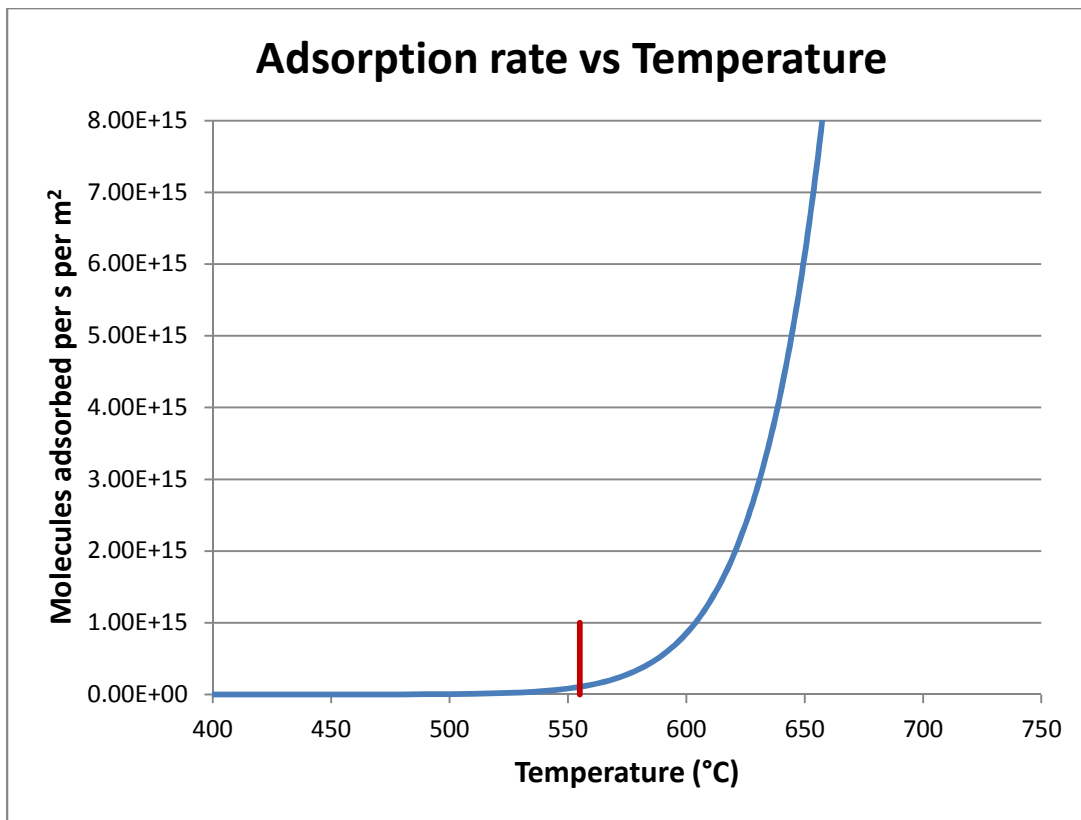


**Figure 28: Adsorption rate as a function of temperature for a 5% blend of silane. The red vertical line represents the temperature at which the high deposition rate area began as shown by Figure 27.**

## Oxidation Performance

Oxidation testing of the non-coated and silicon coated molybdenum substrates was performed by the Corrosion Science and Technology group at the Oak Ridge National Laboratory. [4, 32] Oxidation specimens were coated using the same processing conditions as Mo-Si-5 since these conditions provided the highest coating rate and still maintained an adherent, continuous coating making them the most favorable for a commercial process. Two modified Cahn 1000 thermobalances were used to monitor the mass change of the specimens during oxidation testing which was performed at 550°C in laboratory air for 175 hours. Oxidation performance of the silicon coated specimen was very good with mass gain per surface area of 0.025 mg/cm<sup>2</sup>. Mass gain per surface area of the non-coated molybdenum substrate was ~65 mg/cm<sup>2</sup>, an increase of 3 orders of magnitude in oxidation rate over that of the silicon coated molybdenum. The predominant oxide found was MoO<sub>3</sub> which formed a yellowish scale. It is important to note that EDS mapping, post oxidation testing, (Figure 29) still shows a very distinct interface between the silicon coating and the molybdenum substrate with little to no inter diffusion, indicating that a significant molybdenum silicide layer did not form even after 175 hours at elevated temperature.

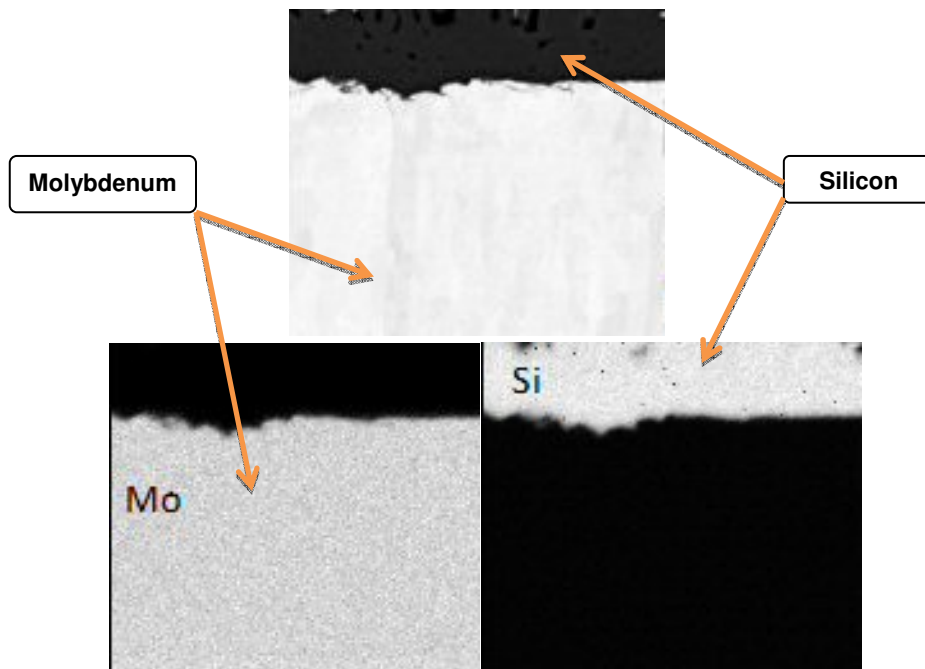


Figure 29: EDS map of Mo/Si interface after oxidation testing at 550°C for 175 hours. [4]

## CHAPTER V

### CONCLUSIONS AND RECOMMENDATIONS

Adherent, continuous silicon coatings were applied to molybdenum substrates using thermally activated CVD techniques and silane gas blended with argon as a precursor. The coatings showed no signs of cracking and performed well as an oxidation barrier with oxidation rates three orders of magnitude less than that of bare molybdenum observed during oxidation tests performed at 550 °C. The low deposition temperature of 575 °C provided low deposition efficiency, but resulted in a discrete silicon layer with little to no inter-diffusion occurring between the molybdenum and silicon. Also, from the XRD pattern, at the low temperatures used the silicon coating deposited was likely either amorphous or nano-crystalline in structure. While the majority of the coating was observed to be uniform and dense, the coating on the outer edges of the substrate, nearest the coating chamber wall, was much thicker and displayed varied porosity depending on the CGF. Lower CGF yielded lower porosity. Modeling of the gas temperature within the coating chamber, and the surface adsorption rate, was performed, and the increased deposition rate on the outer edges of the substrate is thought to be the result of higher gas temperature.

For complete coating of the spherical substrate geometry planned for use in <sup>99</sup>Mo production, a method to agitate the substrates during coating will need to be developed in order to expose all of the substrates surfaces to the coating gases. Also, although the Si coatings did not display any obvious signs of being

overly fragile during handling, durability testing should be completed using a test representative of conditions experienced during service. However, given the successful oxidation protection provided by the coatings produced, silicon coating of the molybdenum material prior to irradiation is considered a good option for <sup>99</sup>Mo production.

## LIST OF REFERENCES



1. *Radioisotopes in Medicine*. 2014; Available from: <http://www.world-nuclear.org/info/non-power-nuclear-applications/radioisotopes/radioisotopes-in-medicine/>.
2. van der Marck, S.C., A.J. Koning, and K.E. Charlton, *The options for the future production of the medical isotope 99Mo*. European Journal of Nuclear Medicine and Molecular Imaging, 2010. **37**(10): p. 1817-1820.
3. Deal, B.E. and A.S. Grove, *General Relationship for the Thermal Oxidation of Silicon*. Journal of Applied Physics, 1965. **36**(12): p. 3770-3778.
4. Jolly, B.C. and S. Dreypondt, *Summary of Silicon Coating of Molybdenum for Elevated Temperature Oxidation Protection*, 2012, Oak Ridge National Laboratory.
5. Doland, C.M. and R.J. Nemanich, *PHASE FORMATION DURING REACTIVE MOLYBDENUM-SILICIDE FORMATION*. Journal of Materials Research, 1990. **5**(12): p. 2854-2864.
6. *ASM Ready Reference: Thermal Properties of Metals*, 2000, ASM International.
7. Claassen, W.A.P. and J. Bloem, *THE NUCLEATION OF CVD SILICON ON SiO<sub>2</sub> AND Si<sub>3</sub>N<sub>4</sub> SUBSTRATES .2. THE SiH<sub>2</sub>Cl<sub>2</sub>-H<sub>2</sub>-N<sub>2</sub> SYSTEM*. Journal of the Electrochemical Society, 1980. **127**(8): p. 1836-1843.
8. Rice, M.J. and K.R. Sarma, *INTERACTION OF CVD SILICON WITH MOLYBDENUM SUBSTRATES*. Journal of the Electrochemical Society, 1981. **128**(6): p. 1368-1373.
9. Pinto, C.R., et al., *Silicon sheet from silane: first results*. Solar Energy Materials and Solar Cells, 2002. **72**(1-4): p. 209-217.
10. Choy, K.L., *Chemical vapour deposition of coatings*. Progress in Materials Science, 2003. **48**(2): p. 57-170.
11. Rath, J.K., *Low temperature polycrystalline silicon: a review on deposition, physical properties and solar cell applications*. Solar Energy Materials and Solar Cells, 2003. **76**(4): p. 431-487.
12. Pierson, H.O., *Handbook of Chemical Vapor Deposition (CVD) - Principles, Technology and Applications (2nd Edition)*, 1999, William Andrew Publishing/Noyes.
13. Blocher, J.M., *Chemical Vapor Deposition*, in *DEPOSITION TECHNOLOGIES FOR FILMS AND COATINGS*. 1982, Noyes Publications: Park Ridge, New Jersey, U.S.A. p. 335-364.
14. Carlsson, J.O. and U. Jansson, *PROGRESS IN CHEMICAL-VAPOR-DEPOSITION*. Progress in Solid State Chemistry, 1993. **22**(4): p. 237-292.
15. Jones, A.C. and M.L. Hitchman, *Chemical Vapor Deposition: Precursors, Processes and Applications*. 2009: RSC Pub.
16. Caputo, A.J., *NERVA FUEL ELEMENT DEVELOPMENT PROGRAM SUMMARY REPORT - JULY 1966 THROUGH JUNE 1972, VAPOR DEPOSITION OF METAL CARBIDES*, 1973, Oak Ridge Y-12 Plant.

17. Gulbransen, E.A. and W.S. Wysong, *THIN OXIDE FILMS ON MOLYBDENUM*. Transactions of the American Institute of Mining and Metallurgical Engineers, 1948. **175**: p. 628-647.
18. Simnad, M. and A. Spilners, *KINETICS AND MECHANISM OF THE OXIDATION OF MOLYBDENUM*. Transactions of the American Institute of Mining and Metallurgical Engineers, 1955. **203**(9): p. 1011-1016.
19. Floquet, N., O. Bertrand, and J.J. Heizmann, *STRUCTURAL AND MORPHOLOGICAL-STUDIES OF THE GROWTH OF MOO3 SCALES DURING HIGH-TEMPERATURE OXIDATION OF MOLYBDENUM*. Oxidation of Metals, 1992. **37**(3-4): p. 253-280.
20. Gulbransen, E.A., K.F. Andrew, and F.A. Brassart, *OXIDATION OF MOLYBDENUM 550-DEGREES-C TO 1700-DEGREES-C*. Journal of the Electrochemical Society, 1963. **110**(9): p. 952-959.
21. Primm, R.T., et al., *Design Study for a Low-Enriched Uranium Core for the High Flux Isotope Reactor, Annual Report for FY 2009, 2010*, Oak Ridge National Laboratory.
22. Atkins, P.W., *Physical Chemistry*. 1990, United States of America: W. H. Freeman and Company.
23. Creighton, J.R. and P. Ho, *Introduction to Chemical Vapor Deposition (CVD)*, in *Chemical Vapor Deposition*, P.J. H., Editor. 2001, ASM International: United States of America.
24. Incropera, F.P., et al., *Fundamentals of Heat and Mass Transfer*. 6th ed. 2007, United States of America: John Wiley & Sons, Inc.
25. Bich, E., J. Millat, and E. Vogel, *The viscosity and thermal conductivity of pure monatomic gases from their normal boiling point up to 5000 K in the limit of zero density and at 0.101325 MPa*. J. Phys. Chem., 1990. **19**(6): p. 1289-1305.
26. *Air Liquide; Gas Encyclopedia*. 2013; Available from: <http://encyclopedia.airliquide.com/encyclopedia.asp?GasID=3&LanguageID=11&CountryID=19>.
27. Ebadian, M.A. and Z.F. Dong, *Forced Convection, Internal Flow in Ducts*, in *Handbook of Heat Transfer*, W.M.H. Rohsenow, J. P.; Cho, Y. I., Editor. 1998, McGraw-Hill: United States of America.
28. Shah, R.K. and M.S. Bhatti, *Laminar Convective Heat Transfer in Ducts*, in *Handbook of Single-Phase Convective Heat Transfer*, S.S. Kakac, R. K.; Aung, W, Editor. 1987, John Wiley & Sons: United States of America.
29. Tao, M., *Growth kinetics and reaction mechanism of silicon chemical vapour deposition from silane*. Thin Solid Films, 1992. **223**: p. 11.
30. Doyle, J., et al., *PRODUCTION OF HIGH-QUALITY AMORPHOUS-SILICON FILMS BY EVAPORATIVE SILANE SURFACE DECOMPOSITION*. Journal of Applied Physics, 1988. **64**(6): p. 3215-3223.

31. Miller, J.H., *Methylsilane Derived SiC Particle Coatings Produced by Fluid-Bed Chemical Vapor Deposition*, in *Materials Science and Engineering* 2006, The University of Tennessee, Knoxville.
32. Dryepontdt, S., *Oxidation of pure Molybdenum in air and He-rich environments at temperatures ranging from 400 to 615C*, 2012, Oak Ridge National Laboratory.

## APPENDIX

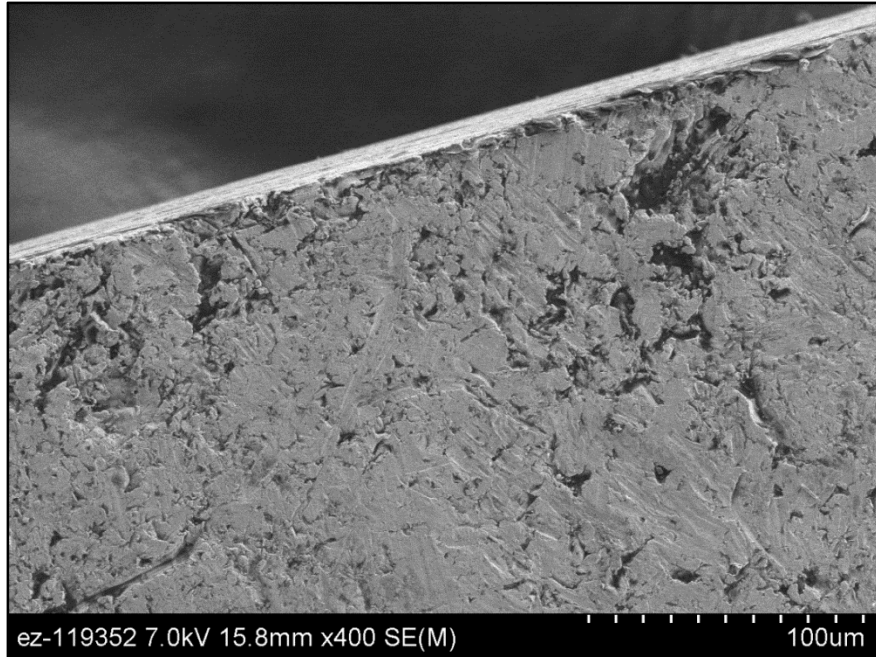


Figure 30: 400X SEM image of surface of uncoated moly taken near center of specimen

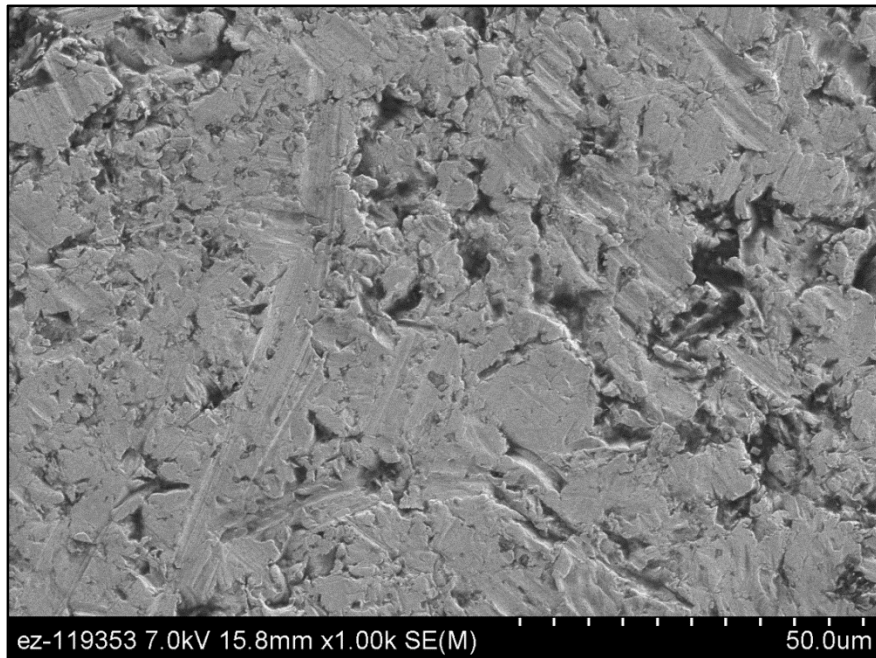


Figure 31: 1000X SEM image of surface of uncoated moly taken near center of specimen

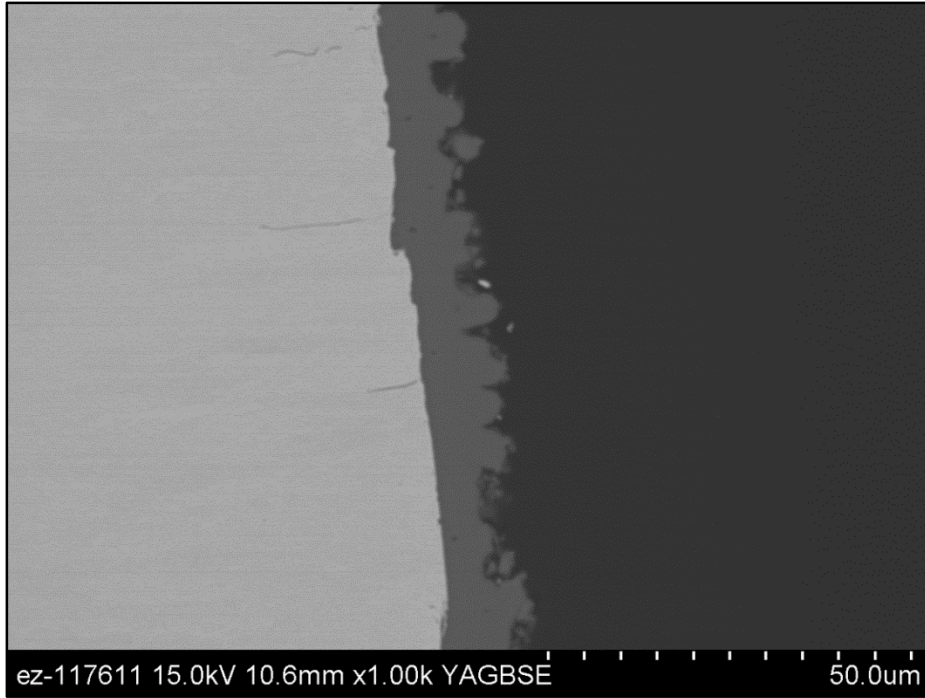


Figure 32: 1000X SEM image of Mo-Si-7 taken near center of cross section

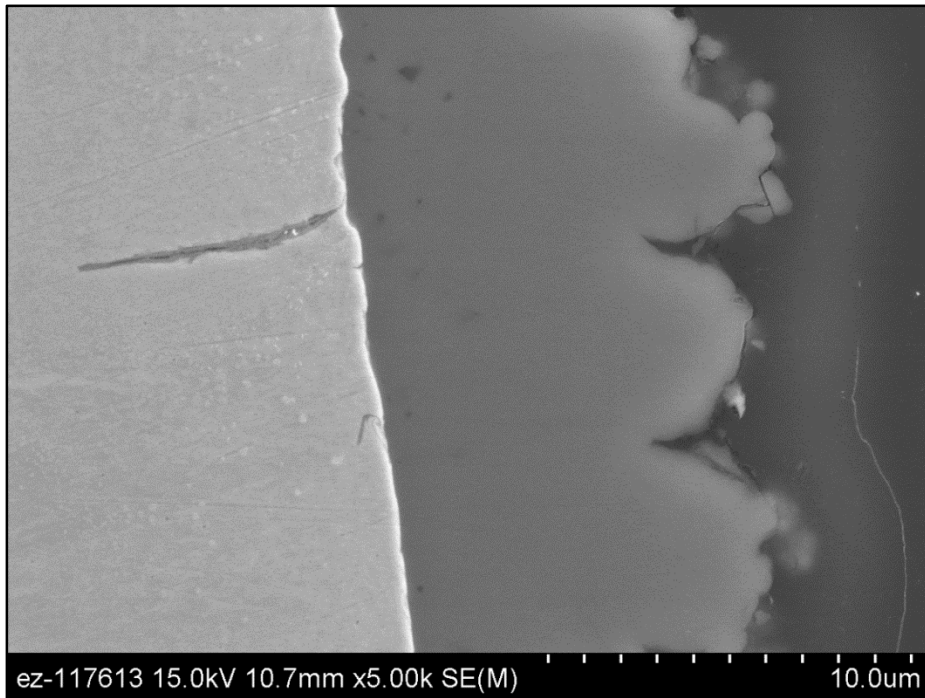


Figure 33: 5000X SEM image of Mo-Si-7 taken near center of cross section

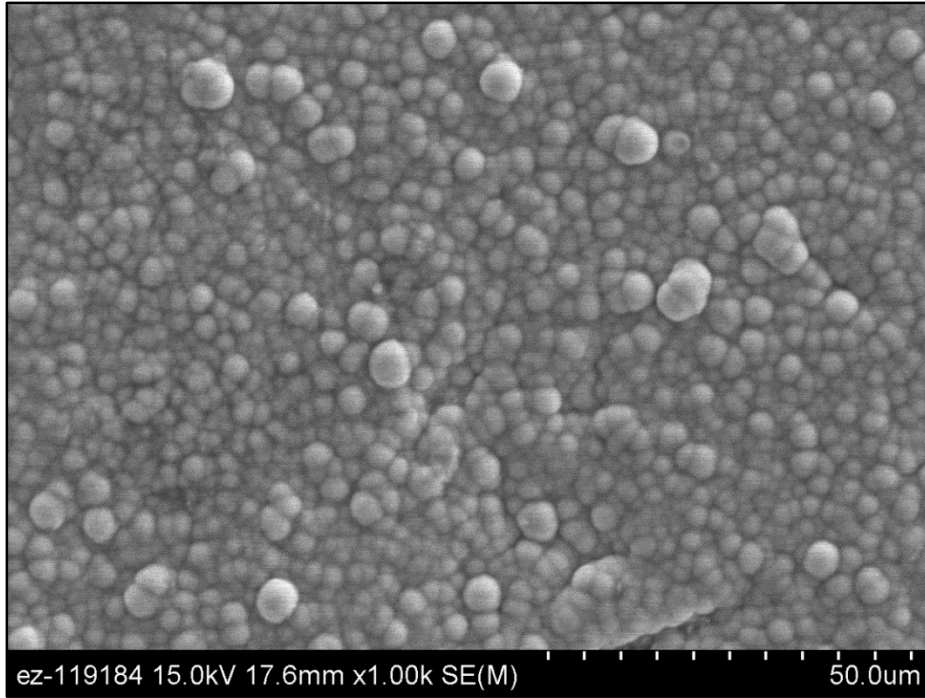


Figure 34: 1000X Surface SEM image of Mo-Si-5 taken near center

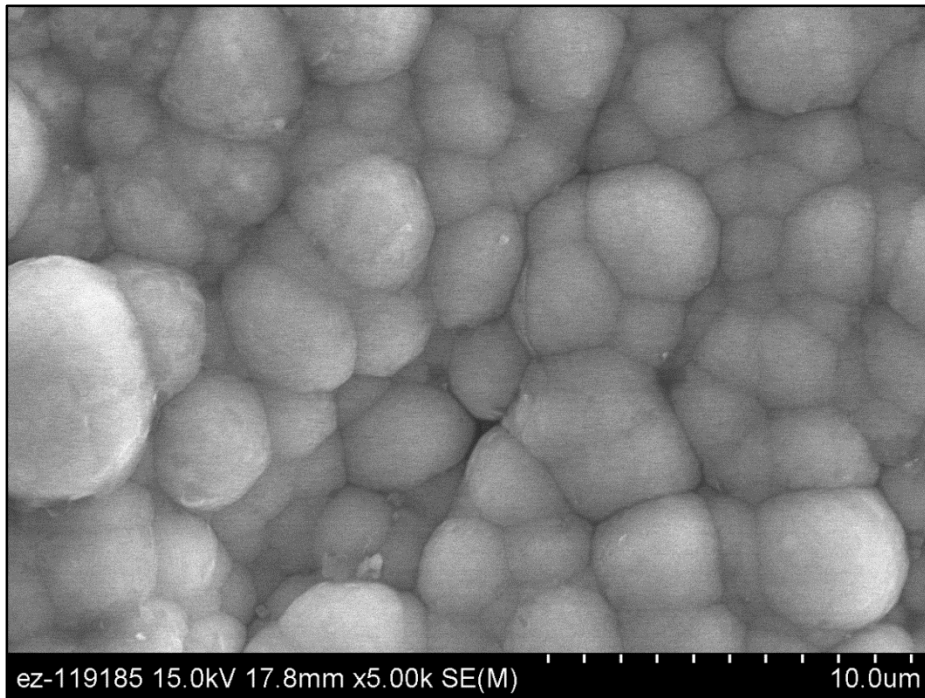


Figure 35: 5000X Surface SEM image of Mo-Si-5 taken near center

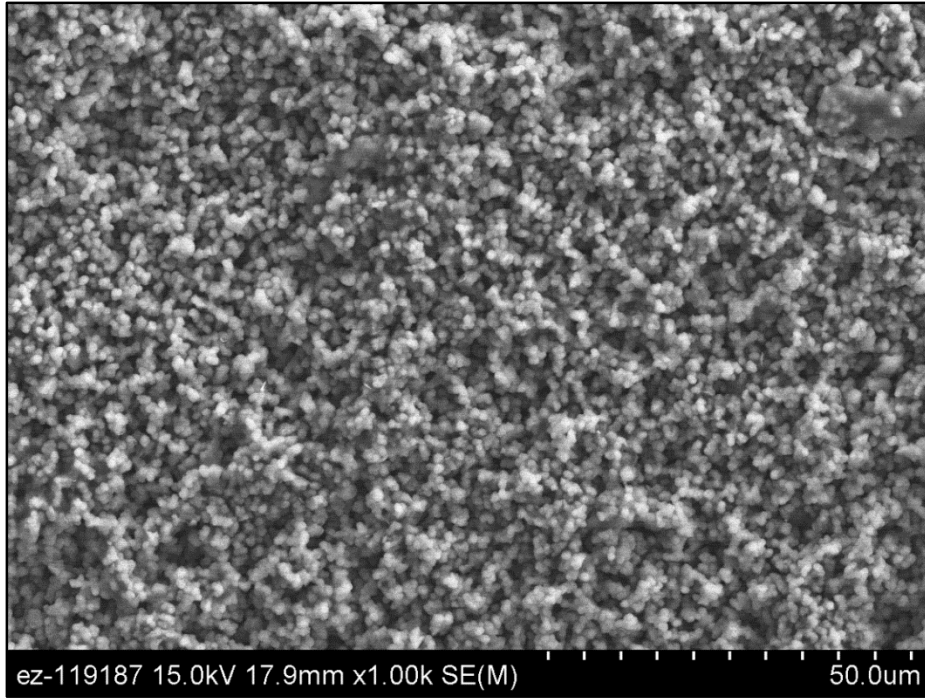


Figure 36: 1000X Surface SEM image of Mo-Si-5 taken near edge

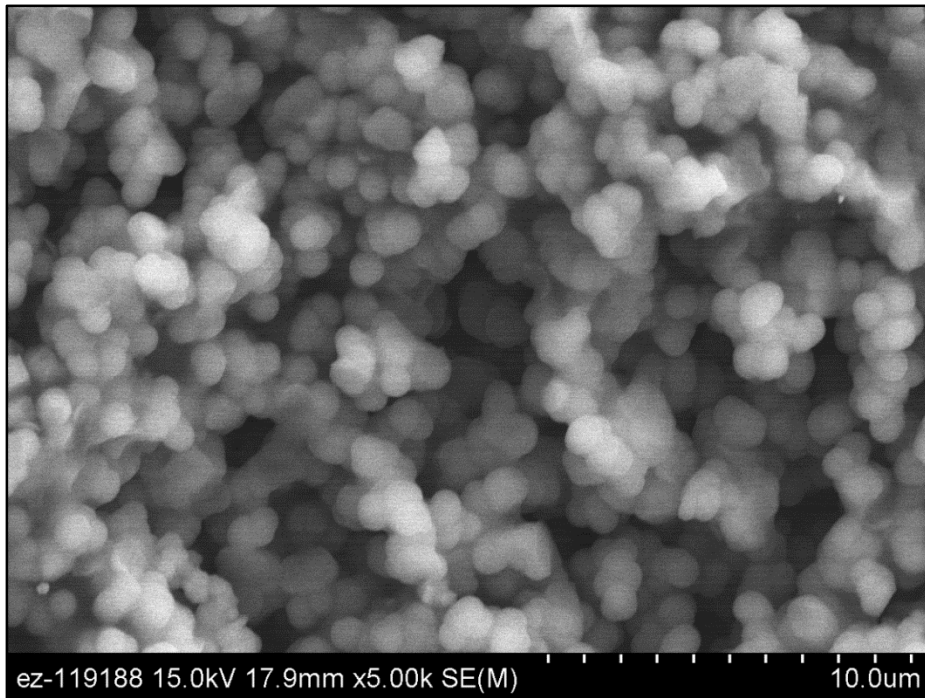


Figure 37: 5000X Surface SEM image of Mo-Si-5 taken near edge



## VITA

Brian Jolly was born in Knoxville Tennessee to parents Michael and Rebecca Jolly. He grew up in Andersonville Tennessee and attended Anderson County High School. After graduation, he attended Pellissippi State Technical Community College where he graduated with an A.A.S in Mechanical Engineering Technology. He then attended East Tennessee State University (ETSU) where he received a B.S. in Manufacturing Engineering Technology. After ETSU, Brian began work at the Oak Ridge National laboratory where he continued his education at the graduate level. Brian graduated with a Master of Science Degree in Materials Science and Engineering from the University of Tennessee in the summer of 2014.